Computers & Fluids 99 (2014) 44–66

Contents lists available at ScienceDirect

Computers & Fluids

journal homepage: www.elsevier.com/locate/compfluid

Large eddy simulation of low Mach number flows using dynamic and orthogonal subgrid scales

Matias Avila [a,b,*], Ramon Codina [c], Javier Principe [d,e]

[a] Centre Internacional de Mètodes Numèrics en Enginyeria (CIMNE), Jordi Girona 1-3, Edifici C1, 08034 Barcelona, Spain
[b] Barcelona Supercomputing Center (BSC), Gran Capità 2-4, Edifici Nexus I Of. 204, 08034 Barcelona, Spain
[c] Universitat Politècnica de Catalunya (UPC), Jordi Girona 1-3, Edici C1, 08034 Barcelona, Spain
[d] Universitat Politècnica de Catalunya (UPC), Urgell 187, 08036 Barcelona, Spain
[e] Centre Internacional de Mètodes Numèrics en Enginyeria (CIMNE), Parc Mediterrani de la Tecnologia, UPC, Esteve Terradas 5, 08860 Castelldefels, Spain

ARTICLE INFO

Article history:
Received 25 April 2013
Received in revised form 25 March 2014
Accepted 2 April 2014
Available online 16 April 2014

Keywords:
Low Mach number flow
LES
Variational Multiscale Method
Turbulent flows
Dynamic subscales

ABSTRACT

Objective: In this article we study the approximation to thermal turbulence from a strictly numerical point of view, without the use of any physical model. The main goal is to analyze the behavior of our numerical method in the large eddy simulation (LES) of thermally coupled turbulent flows at low Mach number.

Methods: Our numerical method is a stabilized finite element approximation based on the variational multiscale method, in which a decomposition of the approximating space into a coarse scale resolvable part and a fine scale subgrid part is performed. Modeling the subscale and taking its effect on the coarse scale problem into account results in a stable formulation. The quality of the final approximation (accuracy, efficiency as LES model) depends on the particular subscale model. The distinctive features of our approach are to consider the subscales as transient and to keep the scale splitting in all the nonlinear terms.

Another important contribution of this work is the extension of the orthogonal subgrid scale method widely tested for incompressible flows to variable density flows, using a density-weighted L^2 product to define the orthogonality of the subscales and the finite element spaces.

Results: Referring to numerical testing, we present numerical results for a laminar testcase validation that shows the dissipative behavior of the different stabilized methods. Then, we present results of the numerical simulation of two turbulent flow problems, the turbulent channel flow with large temperature differences in the wall normal direction at $Re_\tau = 180$, and the turbulent thermally driven cavity with aspect ratio 4. The behavior of the method is evaluated by comparison against results available in the literature obtained using LES and direct numerical simulation (DNS). They are explained based on a careful analysis of the dissipative structure of the method, showing the physical interpretation of the subgrid scale method presented.

conclusion: The material presented here is a clear indication of the potential of the method to model all kinds of turbulent thermally coupled flows. The formulation is the same in laminar and turbulent regimes.

1. Introduction

Turbulent flows with heat transfer arise in many industrial applications, including flows in heat exchangers, combustion systems, etc. In those applications involving considerable variation in fluid properties, design methods based on the assumption of constant properties, as the Boussinesq approximation, generally prove to be inadequate. The present paper is concerned with turbulent flows at low Mach number of an ideal gas subjected to significant density variation, which are described by the compressible Navier–Stokes equations in the low Mach number limit.

Despite the difference in the treatment of the incompressibility, the low Mach number equations present the same mathematical structure as the incompressible Navier–Stokes equations, in the sense that the mechanical pressure is determined from the mass conservation constraint. Consequently the same type of numerical instabilities can be found, namely the problem of compatibility conditions between the velocity and pressure finite element spaces, and the instabilities due to convection dominated flows. These instabilities are avoided by the use of stabilization techniques. In the present work we use a stabilized formulation developed in the context of the variational multiscale (VMS) concept introduced by Hughes [1]. The formulation is based on dynamic

* Corresponding author at: Barcelona Supercomputing Center(BSC), Gran Capità 2-4, Edifici Nexus I Of. 204, Spain. Tel.: +34 93 4054285.
E-mail addresses: matias.avila@bsc.es (M. Avila), ramon.codina@upc.edu (R. Codina), principe@cimne.upc.edu (J. Principe).

http://dx.doi.org/10.1016/j.compfluid.2014.04.003
0045-7930/

and nonlinear subscales, considering the transient nonlinear nature of the problem, see [2]. The idea is to consider the subgrid scale time dependent and to consider its effect in all the nonlinear terms, resulting in extra terms in the final discrete scheme. Important improvements in the discrete formulation of the Navier–Stokes problem have been observed. From a theoretical point of view, the use of transient subgrid scales explains how the stabilization parameter should depend on the time step size and makes space and time discretization commutative. The tracking of the subscales along the nonlinear process provides global mass, momentum and energy conservation. From a practical point of view, the use of time dependent nonlinear subscales results in a more robust and more accurate method (an unusual combination) as shown by numerical experiments [3,4,2]. These developments also opened the door to the use of numerical techniques to cope with the potential instabilities and to model turbulence at the same time, as pointed out in [3,4]. This is a natural step as turbulence is originated by the presence of the nonlinear convective terms, as it is well known. The idea of modeling turbulence using only numerical ingredients actually goes back at least to [5], and the possibility to use the VMS framework for that purpose to [3]. It was fully developed for incompressible flows in [6] for the standard VMS and a complete assessment of different VMS methods is presented in [7]. The application of standard VMS methods to turbulent low Mach number flows was recently presented in [8], where quantitative comparisons against direct numerical simulations are presented.

Large-eddy simulation (LES) of turbulent flows aims at resolving the larger flow structures and modeling the effect of the smaller ones. The distinguishing feature of using VMS as a LES model (VMLES) compared to the traditional LES approach is the use of a variational projection instead of a filter for scale separation. A shortcoming of a LES approach is that it limits convergence rate, due to artificial viscosity effects ($O(h^{4/3})$ in the case of Smagorinsky-type models). This limitation is circumvented using the VMLES point of view and results in a correct behavior in low Reynolds number regimes and in the laminar limit, which is very important to avoid the need of introducing damping functions in laminar regions, e.g. near walls.

A careful analysis of the resulting dissipative structure of the VMS method with nonlinear time dependent subscales was presented in [9,10] for incompressible flows, giving a physical interpretation to the method. In the present work the analysis of the dissipative structure of the VMS method is extended to low Mach compressible flow equations.

The paper is organized as follows. In Section 2, the low Mach number equations and their variational formulation are given. Afterwards, the VMS formulation through dynamic scale splitting is derived in Section 3. Numerical dissipation and kinetic energy conservation are analyzed in Section 4. Numerical examples are presented in Section 5, first a laminar example is solved with the intention of comparing the accuracy and dissipation introduced by the numerical methods presented in this paper against standard stabilization methods available in the literature. The turbulent channel flow problem is solved in Section 5.2, the results are compared against DNS values, and the main dissipative mechanisms are discussed. The last turbulent example is a thermal driven cavity, solved in Section 5.3, where results are compared against DNS results and other LES methods. Conclusions close the paper in Section 6.

2. Formulation of the low Mach equations

2.1. Initial and boundary value problem

Let $\Omega \subset \mathbb{R}^d$, with $d = 2, 3$, be the computational domain in which the flow takes place during the time interval $[0, t_{\text{end}}]$, and let $\partial\Omega$ be its boundary. The initial and boundary value problem to be considered consists of finding a velocity field $\mathbf{u}$, a hydrodynamic pressure field p, a temperature field T, a density ρ and a thermodynamic pressure $p^{\text{th}}(t)$ such that

$$\partial_t \rho + \nabla \cdot (\rho \mathbf{u}) = 0 \text{ in } \Omega, \quad t \in (0, t_{\text{end}}) \tag{1}$$

$$\rho \partial_t \mathbf{u} + \rho \mathbf{u} \cdot \nabla \mathbf{u} - \nabla \cdot (2\mu \boldsymbol{\varepsilon}'(\mathbf{u})) + \nabla p = \mathbf{F} \text{ in } \Omega, \quad t \in (0, t_{\text{end}}) \tag{2}$$

$$\rho c_p \partial_t T + \rho c_p \mathbf{u} \cdot \nabla T - \nabla \cdot (k \nabla T) - \frac{dp^{\text{th}}}{dt} = Q \text{ in } \Omega, \quad t \in (0, t_{\text{end}}) \tag{3}$$

where μ denotes the viscosity, $\boldsymbol{\varepsilon}'(\mathbf{u}) = \boldsymbol{\varepsilon}(\mathbf{u}) - \frac{1}{3}(\nabla \cdot \mathbf{u})\mathbf{I}$ the deviatoric part of the rate of deformation tensor $\boldsymbol{\varepsilon}(\mathbf{u}) = \nabla^s \mathbf{u} = \frac{1}{2}(\nabla \mathbf{u} + \nabla \mathbf{u}^T)$, $\mathbf{I}$ the identity tensor, $\mathbf{F}$ the external force vector, c_p the specific heat coefficient at constant pressure, k the thermal conductivity and Q the heat source. Using the mass conservation statement the temporal and convective terms in (2) can be equivalently written as

$$\rho \partial_t \mathbf{u} + \rho \mathbf{u} \cdot \nabla \mathbf{u} = \partial_t (\rho \mathbf{u}) + \nabla \cdot (\rho \mathbf{u}\mathbf{u})$$

The terms on the left and right hand side are known respectively as non-conservative and conservative temporal and convective terms. A similar observation can be made for the energy Eq. (3).

Properties μ and k are assumed to vary with temperature T according to Sutherland's law:

$$\mu = \left(\frac{T}{T_{\text{ref}}}\right)^{3/2} \left(\frac{T_{\text{ref}} + S}{T + S}\right) \mu_{\text{ref}}, \quad k = \frac{\mu}{\mu_{\text{ref}}} k_{\text{ref}} \tag{4}$$

which uses a reference temperature T_{ref}, a reference viscosity μ_{ref}, the Sutherland temperature S and the reference conductivity k_{ref}. Eqs. (1)–(3) represent the mass, momentum and energy conservation, respectively. Additionally the system is closed by the state equation of ideal gases, relating density ρ, thermodynamic pressure p^{th} and temperature T as

$$\rho = p^{\text{th}} / RT \tag{5}$$

with $R = \frac{\mathcal{R}}{M}$, where $\mathcal{R}$ is the universal gas constant and M the mean molecular mass. Constant specific heats $c_p = 5/2R$ and $c_v = 3/2R$ (perfect gas) are assumed.

These equations must be supplied with initial and boundary conditions. Initial conditions are of the form

$$\mathbf{u} = \mathbf{u}_0 \text{ in } \Omega, \quad t = 0$$
$$T = T_0 \text{ in } \Omega, \quad t = 0$$
$$p^{\text{th}} = p_0^{\text{th}} \text{ in } \Omega, \quad t = 0$$

whereas Dirichlet and Neumann boundary conditions for Eqs. (2) and (3) are

$$\mathbf{u} = \widehat{\mathbf{u}} \text{ on } \Gamma_D^{\mathbf{u}}$$
$$T = \widehat{T} \text{ on } \Gamma_D^T$$
$$(-p\mathbf{I} + 2\mu \boldsymbol{\varepsilon}'(\mathbf{u})) \cdot \mathbf{n} = \mathbf{t}_n \text{ on } \Gamma_N^{\mathbf{u}}$$
$$k \nabla T \cdot \mathbf{n} = q_n \text{ on } \Gamma_N^T$$

where $\mathbf{n}$ is the outer unit normal on the boundary and it is assumed that $\Gamma_D^f \cup \Gamma_N^f = \partial\Omega$, and $\Gamma_D^f \cap \Gamma_N^f = \varnothing$ for $f = T, \mathbf{u}$.

The time dependence of thermodynamic pressure $p^{\text{th}}(t)$ needs to be determined independently of Eqs. (1)–(3). For open flows ($\Gamma_N^{\mathbf{u}} \neq \varnothing$) the thermodynamic pressure must be given by the boundary conditions. The turbulent channel flow is a closed system ($\Gamma_N^{\mathbf{u}} = \varnothing$) where the total mass remains constant over time, and p^{th} may be obtained at each time subject to an integral form of the state equation, implying global mass conservation on domain Ω. This leads to

$$p^{\text{th}} = p_0^{\text{th}} \frac{\int_\Omega \frac{1}{T_0}}{\int_\Omega \frac{1}{T}} \tag{6}$$

where p_0^{th} is the given initial thermodynamic pressure.

2.2. Variational formulation

To obtain a variational formulation for the system (1)–(3), let us denote by $\mathbf{V}$, Q, W the functional spaces where the solution is sought. The corresponding space of (time independent) test functions will be denoted by $\mathbf{V}_0$, Q_0, W_0. Functions belonging to these spaces vanish on the part of the boundary where Dirichlet conditions are imposed. We also introduce the notation $(\cdot,\cdot) \equiv (\cdot,\cdot)_\Omega$ and $(\cdot,\cdot)_\Gamma$ for the L^2-inner product on Ω and Γ, respectively. In some instances we will abuse the notation and use this symbol for the integral of the product of two functions, not necessarily square-integrable.

Using this notation the weak form of the problem consists of finding $(\mathbf{u}, p, T) \in \mathbf{V} \times Q \times W$ such that

$$(\partial_t \rho, q) + (\nabla \cdot (\rho \mathbf{u}), q) = 0 \quad \forall q \in Q_0 \tag{7}$$

$$c(\rho, \mathbf{u}, \mathbf{u}, \mathbf{v}) + (2\mu\boldsymbol{\varepsilon}'(\mathbf{u}), \nabla^s \mathbf{v}) - (p, \nabla \cdot \mathbf{v}) = (\mathbf{F}, \mathbf{v}) + (\mathbf{t}_n, \mathbf{v})_{\Gamma_N^{\mathbf{u}}} \quad \forall \mathbf{v} \in \mathbf{V}_0 \tag{8}$$

$$d(\rho c_p, \mathbf{u}, T, w) + (k\nabla T, \nabla w) - (d_t p^{\text{th}}, w) = (Q, w) + (q_n, w)_{\Gamma_N^T} \quad \forall w \in W_0 \tag{9}$$

where $c(\rho, \mathbf{u}, \mathbf{u}, \mathbf{v})$ is the form coming from the convective and temporal derivative terms, which can be defined in different ways, namely,

$$c_{\text{nc}}(\rho, \mathbf{a}, \mathbf{u}, \mathbf{v}) = \int_\Omega (\rho \partial_t \mathbf{u} + \rho \mathbf{a} \cdot \nabla \mathbf{u}) \cdot \mathbf{v} \quad \text{Non conservative form}$$

$$c_{\text{c}}(\rho, \mathbf{a}, \mathbf{u}, \mathbf{v}) = \int_\Omega \partial_t(\rho \mathbf{u}) \cdot \mathbf{u} - \int_\Omega \rho \mathbf{a} \mathbf{u} : \nabla \mathbf{v} + \int_{\partial\Omega} \rho (\mathbf{n} \cdot \mathbf{a})(\mathbf{u} \cdot \mathbf{v}) \quad \text{Conservative form}$$

These forms are equivalent at the continuous level due to the continuity Eq. (1), and they satisfy

$$c_{\text{nc}}(\rho, \mathbf{a}, \mathbf{u}, \mathbf{u}) = \partial_t \int_\Omega k + \int_{\partial\Omega} \mathbf{n} \cdot \mathbf{a} k - \frac{1}{2} \int_\Omega (\partial_t \rho + \nabla \cdot (\rho \mathbf{a}))|\mathbf{u}|^2 \tag{10}$$

$$c_{\text{c}}(\rho, \mathbf{a}, \mathbf{u}, \mathbf{u}) = \partial_t \int_\Omega k + \int_{\partial\Omega} \mathbf{n} \cdot \mathbf{a} k + \frac{1}{2} \int_\Omega (\partial_t \rho + \nabla \cdot (\rho \mathbf{a}))|\mathbf{u}|^2 \tag{11}$$

where $k = \frac{1}{2}\rho \mathbf{u} \cdot \mathbf{u}$ is the kinetic energy per unit of volume. The continuity equation guarantees that the last term in the right hand side of (10) and (11) vanishes when $\mathbf{a} = \mathbf{u}$. Then the term $c(\rho, \mathbf{u}, \mathbf{u}, \mathbf{u})$ accounts for kinetic energy variation inside the domain Ω and kinetic energy flux through the boundaries. However, as it will be discussed in Section 4, these properties are lost at the discrete level, which motivates the introduction of a skew-symmetric form

$$c_{\text{ss}}(\rho, \mathbf{a}, \mathbf{u}, \mathbf{v}) = \frac{1}{2}(c_{\text{c}}(\rho, \mathbf{a}, \mathbf{u}, \mathbf{v}) + c_{\text{nc}}(\rho, \mathbf{a}, \mathbf{u}, \mathbf{v})) \tag{12}$$

that is again equivalent to (10) and (11) (thanks to the continuity) and satisfies

$$c_{\text{ss}}(\rho, \mathbf{a}, \mathbf{u}, \mathbf{u}) = \partial_t \int_\Omega k + \int_{\partial\Omega} \mathbf{n} \cdot \mathbf{a} k \tag{13}$$

for any ρ, $\mathbf{a}$ and $\mathbf{u}$. Similar equivalent definitions are introduced for the convective temporal derivative in the energy equation $d(\rho c_p, \mathbf{u}, T, w)$. At the discrete level the equivalence between these forms is lost.

The term "skew-symmetric" means that $c_{\text{ss}}(\rho, \mathbf{a}, \mathbf{u}, \mathbf{u}) = 0$ for steady flows and velocity vanishing over the boundaries. It can be said that the skew-symmetric form is conservative *a priori* in the kinetic energy equation. This formulation was used in incompressible turbulent flows [11,7] with the objective of diminishing artificial numerical dissipation. Its actual influence in the kinetic energy budget of incompressible flows is shown in [7]. In this work we use the skew-symmetric form of the convective term in the momentum equation in order to ensure conservation of kinetic energy, whereas we choose for convenience the nonconservative form in the energy equation.

3. Space discretization

Let us consider a finite element partition $\{K\}$ of the computational domain Ω, from which we can construct finite element spaces for the velocity, pressure and temperature in the usual manner. We will denote them by $\mathbf{V}_h \subset \mathbf{V}$, $Q_h \subset Q$ and $W_h \subset W$, respectively. We assume zero Dirichlet boundary conditions to simplify the presentation. Note that in the spaces introduced time has not yet been discretized.

3.1. Scale splitting

Let us split the continuous space $\mathbf{Y} = \mathbf{V} \times Q \times W$ as $\mathbf{Y} = \mathbf{Y}_h \oplus \widetilde{\mathbf{Y}}$, where $\widetilde{\mathbf{Y}} = \widetilde{V} \times \widetilde{Q} \times \widetilde{W}$ is the subgrid space, that can be in principle any space to complete $\mathbf{Y}_h = \mathbf{V}_h \times Q_h \times W_h$ in $\mathbf{Y}$. The continuous unknowns are split as

$$\mathbf{u} = \mathbf{u}_h + \widetilde{\mathbf{u}} \tag{14}$$

$$p = p_h + \widetilde{p} \tag{15}$$

$$T = T_h + \widetilde{T} \tag{16}$$

where the components with subscripts h belong to the corresponding finite element spaces, and the components with the ˜ correspond to the subgrid space. These additional components are what we will call subscales.

Our particular approach is to keep the time dependency of these subscales and keep the previous decompositions (14)–(16) in *all* the terms of the variational problem (7)–(9). The only approximation we will make for the moment is to assume that the subscales vanish on the element boundaries, ∂K. Substituting decompositions (14)–(16) in the variational problem (7)–(9), taking the tests functions in the corresponding finite element spaces and integrating some terms by parts in order to avoid spatial derivatives of the subscales, the discrete problem consists of finding $(\mathbf{u}_h, T_h, p_h) \in \mathbf{V}_h \times Q_h \times W_h$ such that

$$(\partial_t \rho^h, q_h) - (\rho^h \mathbf{u}_h, \nabla q_h) + (\rho^h \mathbf{n} \cdot \mathbf{u}_h, q_h)_{\partial\Omega} - (\rho^h \widetilde{\mathbf{u}}, \nabla q_h) = 0 \tag{17}$$

$$\begin{aligned} &c(\rho^h, \mathbf{u}_h + \widetilde{\mathbf{u}}, \mathbf{u}_h, \mathbf{v}_h) + (2\mu\boldsymbol{\varepsilon}'(\mathbf{u}_h), \nabla^s \mathbf{v}_h) - (p_h, \nabla \cdot \mathbf{v}_h) \\ &\quad - (\widetilde{p}, \nabla \cdot \mathbf{v}_h) + (\partial_t(\rho^h \widetilde{\mathbf{u}}), \mathbf{v}_h) \\ &\quad - \left(\widetilde{\mathbf{u}}, \rho^h(\mathbf{u}_h + \widetilde{\mathbf{u}}) \cdot \nabla \mathbf{v}_h + \nabla^h \cdot (2\mu\boldsymbol{\varepsilon}(\mathbf{v}_h))\right)_h \\ &\quad = (\mathbf{F}, \mathbf{v}_h) \end{aligned} \tag{18}$$

$$\begin{aligned} &d(\rho^h c_p, \mathbf{u}_h + \widetilde{\mathbf{u}}, T_h, w_h) + (k\nabla T_h, \nabla w_h) + \left(c_p \partial_t\left(\rho^h \widetilde{T}\right), w_h\right) \\ &\quad - \left(\widetilde{T}, \rho^h c_p(\mathbf{u}_h + \widetilde{\mathbf{u}}) \cdot \nabla w_h + \nabla^h \cdot (k\nabla w_h)\right) - (d_t p^{\text{th}}, w_h) \\ &\quad = (Q, w_h) \end{aligned} \tag{19}$$

for any test functions $(\mathbf{v}_h, q_h, w_h) \in \mathbf{V}_{0,h} \times Q_{0,h} \times W_{0,h}$, where

$$\rho^h = p^{\text{th}} / R(T_h + \widetilde{T}) \tag{20}$$

is obtained applying the scale splitting to the state Eq. (5). We stress that the unknown of the problem is (either the finite element or subgrid) temperature and (20) should be understood as notation (i.e. ρ^h could be replaced elsewhere by its definition but that would make reading more difficult). The temperature scale splitting is also applied to the viscosity Eq. (4). The symbol ∇^h in Eqs. (18) and (19) indicates that the divergence is taken in the finite element interiors, and the subscript h in the corresponding inner product indicates that it is performed elementwise. After a proper by parts integration of the discrete equations we made some manipulation to arrive to the discrete formulation of momentum and energy Eqs. (18) and

(19) avoiding the presence of spatial derivatives of the subscale component. After scale splitting the continuous mass conservation Eq. (7) can be written as

$$(\partial_t \rho^h, q) = -(\nabla \cdot (\rho^h(\mathbf{u}_h + \tilde{\mathbf{u}})), q)$$

We replaced this continuous form of the mass conservation equation into the momentum and energy equations after performing some integrations by parts. Those replacements are crucial to account for the subscales in all the nonlinear terms. In particular, we have replaced $(\tilde{\mathbf{u}}, \nabla \cdot (\rho^h(\mathbf{u}_h + \tilde{\mathbf{u}}))\mathbf{v}_h)$ by $-(\tilde{\mathbf{u}}, \partial_t \rho^h \mathbf{v}_h)$ in the momentum equation, and $\left(\tilde{T}, \nabla \cdot (\rho^h(\mathbf{u}_h + \tilde{\mathbf{u}}))w_h\right)$ by $-\left(\tilde{T}, \partial_t \rho^h w_h\right)$ in the energy equation, under the assumption that $\tilde{\mathbf{u}} \cdot \mathbf{v}_h \in Q$ and $\tilde{T} w_h \in Q$.

In order to give a closure to system (17)–(20) we need to define how the subscales $\tilde{\mathbf{u}}$, $\tilde{p}$ and $\tilde{T}$ are computed, which will be discussed in the rest of the section. However, we would like to point out that, once the velocity subscale is approximated in the momentum Eq. (18), it provides additional terms to those that appear in classical stabilized finite element methods. These are non standard terms in the sense that they are usually neglected and appear because we keep the scale splitting also in nonlinear terms. The terms involving the velocity subgrid scale arising from the convective term in the momentum equation, namely $(\rho^h \tilde{\mathbf{u}} \cdot \nabla \mathbf{u}_h, \mathbf{v}_h)$ $-(\tilde{\mathbf{u}}, \rho^h(\mathbf{u}_h + \tilde{\mathbf{u}}) \cdot \nabla \mathbf{v}_h)$, can be understood as the contribution from the Reynolds- and cross- stress terms of a LES approach. Therefore, modeling $\tilde{\mathbf{u}}$ implies modeling the subgrid scale tensor. Similar comments apply to the energy Eq. (19), in which case the terms involving the velocity and temperature subgrid scales arising from the convective term are $(\rho^h c_p \tilde{\mathbf{u}} \cdot \nabla T_h, w_h)$ $-\left(\tilde{T}, \rho^h c_p(\mathbf{u}_h + \tilde{\mathbf{u}}) \cdot \nabla w_h\right)$.

To get the final numerical scheme we approximate the subscales in the element interiors. The equations for the subscales are obtained by projecting the original equations onto their corresponding spaces $\tilde{\mathbf{Y}}$. If $\tilde{P}$ denotes the L^2-projection onto any of these spaces, the subscale equations are written as

$$\tilde{P}\left(\rho^h \nabla \cdot \tilde{\mathbf{u}} - \rho^h \beta^h (\mathbf{u}_h + \tilde{\mathbf{u}}) \cdot \nabla \tilde{T}\right) = \tilde{P}(R_c) \tag{21}$$

$$\tilde{P}(\partial_t(\rho^h \tilde{\mathbf{u}}) + \nabla \cdot (\rho^h(\mathbf{u}_h + \tilde{\mathbf{u}})\tilde{\mathbf{u}}) - \nabla \cdot (2\mu \boldsymbol{\varepsilon}'(\tilde{\mathbf{u}})) + \nabla \tilde{p}) = \tilde{P}(\mathbf{R}_m) \tag{22}$$

$$\tilde{P}\left(c_p \partial_t\left(\rho^h \tilde{T}\right) + c_p \nabla \cdot \left(\rho^h(\mathbf{u}_h + \tilde{\mathbf{u}})\tilde{T}\right) - \nabla \cdot \left(k \nabla \tilde{T}\right)\right) = \tilde{P}(R_e) \tag{23}$$

where the residuals of mass, momentum and energy equations are respectively

$$R_c = -\partial_t \rho^h - \rho^h \nabla \cdot \mathbf{u}_h + \rho^h \beta^h (\mathbf{u}_h + \tilde{\mathbf{u}}) \cdot \nabla T_h \tag{24}$$

$$\mathbf{R}_m = \mathbf{F} - \rho^h \partial_t \mathbf{u}_h - \rho^h (\mathbf{u}_h + \tilde{\mathbf{u}}) \cdot \nabla \mathbf{u}_h + \nabla \cdot (2\mu \boldsymbol{\varepsilon}'(\mathbf{u}_h)) - \nabla p_h \tag{25}$$

$$R_e = Q + d_t p^{\text{th}} - \rho^h c_p \partial_t T_h - \rho^h c_p (\mathbf{u}_h + \tilde{\mathbf{u}}) \cdot \nabla T_h + \nabla \cdot (k \nabla T_h) \tag{26}$$

and

$$\beta^h = \left(T_h + \tilde{T}\right)^{-1} \tag{27}$$

is the thermal expansion coefficient, which appears when gradients of the density are computed. As in the case of Eq. (20) we stress that the unknown of the problem is (either the finite element or subgrid) temperature and (27) should be understood as a notation (i.e. β^h could be replaced elsewhere by its definition).

The final form of (21) and (24) is different to that of (17) because the subscale equations are not integrated, and density gradients have been computed explicitly. The temporal and convective terms of the momentum and energy subscale equations are written in conservative form. This form will be convenient for the development of the orthogonal subscale approximation, and also will permit to ease the implementation after grouping in the finite element equations the following terms

$$(\rho^h \partial_t \tilde{\mathbf{u}}, \mathbf{v}_h) + (\tilde{\mathbf{u}}, \partial_t \rho^h \mathbf{v}_h) = (\partial_t(\rho^h \tilde{\mathbf{u}}), \mathbf{v}_h)$$
$$\left(\rho^h \partial_t \tilde{T}, w_h\right) + \left(\tilde{T}, \partial_t \rho^h w_h\right) = \left(\partial_t\left(\rho^h \tilde{T}\right), w_h\right)$$

asi it will be shown the right-hand-side terms are zero for the orthogonal subscale approximation method.

3.2. Approximation of the subscales

Up to this point the only approximation introduced is to assume that the subscales vanish on the element boundaries. We adopt a simple approximation which consists in replacing the (spatial) differential operator by an algebraic operator which can be easily inverted. The differential Eqs. (21)–(23) over each element domain K can be written in vectorial form as

$$\tilde{P}\left(\partial_t(\mathbf{M}\tilde{\mathbf{U}}) + \mathcal{L}\tilde{\mathbf{U}}\right) = \tilde{P}(\mathbf{R}) \quad \text{in} \quad K \tag{28}$$

where $\tilde{\mathbf{U}} \equiv \left(\tilde{\mathbf{u}}, \tilde{p}, \tilde{T}\right)$, $\mathcal{L}$ is a nonlinear spatial differential vector operator, $\mathbf{M}$ is the $(d+2) \times (d+2)$ diagonal matrix $\mathbf{M} = \text{diag}(\rho^h \mathbf{I}_d, 0, \rho^h c_p)$, where $\mathbf{I}_d$ is the $d \times d$ identity matrix, and $\mathbf{R} \equiv (\mathbf{R}_m, R_c, R_e)$. In the present paper we will consider two options. First, we will take the space of subscales as that of the residuals, that is, we will consider $\tilde{P} = I$ (the identity) when applied to the finite element residuals. We will also consider $\tilde{P}$ as the projection onto the space orthogonal to the finite element space, advocated in [3] for incompressible flows. This method presents some advantages for incompressible flows, like better accuracy, a clear identification of the energy transfer mechanisms between the finite element scales and the subscales [10], as well as improved stability and convergence estimates for transient Stokes and incompressible flows [12,13]. The development of the Orthogonal Subscale Stabilization method for low Mach number equations will be detailed in the next subsection, expecting to present some of the advantages achieved for incompressible flows when extended to the low Mach number problem. Since we will consider dynamic subgrid scales, we will label DOSS the method to be described.

We consider the algebraic approximation $\mathcal{L} \approx \boldsymbol{\tau}^{-1}$ in each K, where $\boldsymbol{\tau}$ is an $(d+2) \times (d+2)$ diagonal matrix. Taking $\boldsymbol{\tau} = \text{diag}(\tau_m \mathbf{I}_d, \tau_c, \tau_e)$ the approximation to the subscales Eqs. (21)–(23) within each element of the finite element partition reads

$$\tau_c^{-1} \tilde{p} = R_c + p_{\text{ort}} = R'_c \tag{29}$$

$$\partial_t(\rho^h \tilde{\mathbf{u}}) + \tau_m^{-1} \tilde{\mathbf{u}} = \mathbf{R}_m + \mathbf{u}_{\text{ort}} = \mathbf{R}'_m \tag{30}$$

$$c_p \partial_t(\rho^h \tilde{T}) + \tau_e^{-1} \tilde{T} = R_e + T_{\text{ort}} = R'_e \tag{31}$$

where p_{ort}, $\mathbf{u}_{\text{ort}}$ and T_{ort} are functions L^2- orthogonal to the subscale space. After the approximation $\mathcal{L} \approx \boldsymbol{\tau}^{-1}$, Eqs. (29)–(31) become a set of ordinary differential–algebraic equations at each integration point. The stabilization parameters can be motivated by an approximated Fourier analysis performed in [3]. The same analysis can be repeated for the present variable-density equation system to obtain

$$\tau_c = \frac{h^2}{c_1 \rho^h \tau_m} = \frac{\mu}{\rho^h} + \frac{c_2}{c_1} |\mathbf{u}_h + \tilde{\mathbf{u}}| h \tag{32}$$

$$\tau_m^{-1} = c_1 \frac{\mu}{h^2} + c_2 \frac{\rho^h |\mathbf{u}_h + \tilde{\mathbf{u}}|}{h} \tag{33}$$

$$\tau_e^{-1} = c_1 \frac{k}{h^2} + c_2 \frac{\rho^h c_p |\mathbf{u}_h + \tilde{\mathbf{u}}|}{h} \tag{34}$$

where h is the element size and c_1 and c_2 are algorithmic constants whose values are $c_1 = 12$ and $c_2 = 2$ for linear elements in the

numerical experiments to be presented. Those values are very important for the design of the stabilization parameters. An interpretation for coefficients c_1 and c_2 was found from a Fourier analysis in [3], implying the restriction $c_2^2 \leqslant c_1$. Note that larger c_1 values imply smaller τ_c, τ_m and τ_e, leading to a less dissipative scheme (as explained in Section 4).

The Reynolds number based on the element length $\mathrm{Re}_h = \frac{\rho^h |\mathbf{u}_h + \widetilde{\mathbf{u}}| h}{\mu}$ gives the relation between the current mesh size h to Kolmogorov's length scale λ, defined such that the associated Reynolds number is 1. Taking $h \approx \lambda$ ($\mathrm{Re}_h \approx 1$) is the needed mesh discretization to perform a direct numerical simulation (DNS), or to avoid numerical oscillations due to dominant convective terms when using the Galerkin approximation. When solving turbulent flows using LES models or stabilized finite elements, generally $\mathrm{Re}_h \gg 1$ away from the walls. When this happens it is very important to introduce numerical dissipation in order to obtain a stable numerical formulation. It is observed in Eqs. (32)–(34) that when $\mathrm{Re}_h \gg 1$ the values of τ_m and τ_e are barely sensitive to c_1 while τ_c is very sensitive to c_1. We have found in the numerical experiments that increasing c_1 decreases considerably the total numerical dissipation. This is due to the sensibility on τ_c of the total amount of numerical dissipation. When $\mathrm{Re}_h \leqslant 1$ (in viscous dominant regions close to boundary layers) $\tau_c \to \mu/\rho^h$, introducing a volumetric viscosity μ for incompressible flows. We have observed that to define τ_c such $\tau_c \to C\mu/\rho^h$ as $\mathrm{Re}_h \to 0$ with $C \geqslant 1$ deteriorates the boundary layer behavior if C differs from 1, giving very inaccurate results.

Eqs. (29)–(31) form a dynamic system of nonlinear equations at each integration point. Before discretizing in time, we cannot go any further than saying that the problem consists in solving (17)–(20) together with (29)–(31). Similar conclusions were obtained for incompressible flows in [7], where the possibility of using $\widetilde{p} = 0$ is also analyzed.

Remark 1. Solutions to the nonlinear subscale Eqs. (30) and (31) display a dynamic behavior which may be radically different from the linear one. Due to the nonlinear modeling of these equations, the subscales must be dynamic, its time derivative cannot be neglected, in order to avoid a possible lack of uniqueness in their calculations. An easy example showing this lack of uniqueness occurs when $|\widetilde{\mathbf{u}}| \gg |\mathbf{u}_h|$ and only the convective term is relevant ($\mathrm{Re}_h \gg 1$), yielding

$$c_1 \frac{|\widetilde{\mathbf{u}}|}{h} \widetilde{\mathbf{u}} \approx \widetilde{\mathbf{u}} \cdot \nabla \mathbf{u}_h, \quad c_1 \frac{|\widetilde{\mathbf{u}}|}{h} \widetilde{T} \approx \widetilde{\mathbf{u}} \cdot \nabla T_h$$

being $\widetilde{\mathbf{u}}$, $\widetilde{T}$ and $-\widetilde{\mathbf{u}}$, $-\widetilde{T}$ solutions of the problem.

3.2.1. DASGS and DOSS methods

The starting point of our developments has been the decomposition of the continuous space $\mathbf{Y}$ as $\mathbf{Y} = \mathbf{Y}_h \oplus \widetilde{\mathbf{Y}}$. There are many possibilities to choose $\widetilde{\mathbf{Y}}$. The easiest choice is to consider the space of subscales as that of the residuals, that is, to consider $\widetilde{P} = I$ (the identity) when applied to the finite element residuals. That amounts to take $p_{\mathrm{ort}}, \mathbf{u}_{\mathrm{ort}}$ and T_{ort} equal zero in Eqs. (29)–(31). This yields the common choice of taking the subscales directly proportional to the finite element residual. We will call this approach Dynamic Algebraic SubGrid Scale (DASGS) method, the time-dependence of the subscales being a characteristic feature of our approach.

Another possibility consists in taking precisely $\widetilde{\mathbf{Y}} = Y \cap Y_h^{\perp}$, respect to the inner product $(u, v)_\rho = (u, \rho^h v)$. Note that as the density ρ^h is time dependent, then the subscale space $\widetilde{\mathbf{Y}}$ will also depend on time. From the previous definition, any subscale function $\widetilde{\mathbf{u}}$ must satisfy the following relationship

$$(\rho^h \widetilde{\mathbf{u}}, \mathbf{u}_h) = 0 \quad \forall \mathbf{u}_h \in \mathbf{V}_h \tag{35}$$

We need to find the appropriate p_{ort}, $\mathbf{u}_{\mathrm{ort}}$ and T_{ort} in (29)–(31) to satisfy the orthogonal relationship (35). In what follows we will show the procedure of finding $\mathbf{u}_{\mathrm{ort}}$ in the subscale momentum Eq. (30). The same procedure is applied to the energy and pressure subscale equations to determine p_{ort} and T_{ort}. Projecting expression (30) over the finite element space, and satisfying the orthogonality condition (35) we get that

$$(\partial_t(\rho^h \widetilde{\mathbf{u}}), \mathbf{v}_h) = 0 = (\mathbf{R}_m + \mathbf{u}_{\mathrm{ort}} - \tau_m^{-1} \widetilde{\mathbf{u}}, \mathbf{v}_h) \quad \forall \mathbf{v}_h \in \mathbf{V}_h \tag{36}$$

from where it follows that $\mathbf{u}_{\mathrm{ort}}$ is the following projection onto the finite element space with respect to the L^2-inner product, denoted by P_h:

$$\mathbf{u}_{\mathrm{ort}} = P_h(-\mathbf{R}_m + \tau_m^{-1} \widetilde{\mathbf{u}})$$

Replacing in (30) we find the momentum subscale equation

$$\partial_t(\rho^h \widetilde{\mathbf{u}}) = P_h^{\perp}(\mathbf{R}_m - \tau_m^{-1} \widetilde{\mathbf{u}}) \tag{37}$$

where $P_h^{\perp} = I - P_h$, and I is the identity in $\mathbf{V}_h$. This differential equation has been found to be unstable in the numerical experiments because the directional vectors $P_h^{\perp}(\tau_m^{-1} \widetilde{\mathbf{u}})$ and $\widetilde{\mathbf{u}}$ do not have the same directions. In case they have opposite directions, the solution to Eq. (37) grows exponentially in time and the whole method becomes unstable. To overcome that problem we assume that $\rho^h \tau_m$ has a smooth variation from element to element, thus we can approximate $P_h(\tau_m^{-1} \widetilde{\mathbf{u}}) \approx (\rho^h \tau_m)^{-1} P_h(\rho^h \widetilde{\mathbf{u}}) = 0$. After applying the same approximation to Eq. (31), and assuming $\widetilde{p} \in Q_h^{\perp}$ the orthogonal subscale equations will read

$$\widetilde{p} = \tau_c P_h^{\perp}(R_c) \tag{38}$$

$$\partial_t(\rho^h \widetilde{\mathbf{u}}) + \tau_m^{-1} \widetilde{\mathbf{u}} = P_h^{\perp}(\mathbf{R}_m) \tag{39}$$

$$c_p \partial_t(\rho^h \widetilde{T}) + \tau_e^{-1} \widetilde{T} = P_h^{\perp}(R_e) \tag{40}$$

The Dynamic Orthogonal Subscale Stabilization (DOSS) method consists in solving the finite element Eqs. (17)–(19) together with the subscale Eqs. (38)–(40). The terms $(\partial_t(\rho^h \widetilde{\mathbf{u}}), \mathbf{v}_h)$ and $(\partial_t(\rho^h \widetilde{T}), w_h)$ vanish in the finite element problem due to the L^2 orthogonality with weight ρ^h between $\widetilde{\mathbf{Y}}$ and $\mathbf{Y}_h$, and leads to an easier implementation of the problem. For incompressible flows this property is responsible of getting a scale separation between the finite element components and the subscales in the kinetic energy balance [11]. The transient terms $\rho^h \partial_t \mathbf{u}_h$ and $\rho^h c_p \partial_t T_h$ are neglected from the energy and momentum residuals $\mathbf{R}_m$ and R_e in the subscale Eqs. (39) and (40), again because they are L^2-orthogonal with weight ρ^h to the subscale space, that is to say, $\widetilde{P}(\rho^h \partial_t \mathbf{u}_h) = 0$ and $\widetilde{P}(\rho^h \partial_t T_h) = 0$ in the original subscale Eqs. (22) and (23). Note however that by virtue of approximation $P_h(\tau_m^{-1} \widetilde{\mathbf{u}}) \approx 0$ we have $\widetilde{P}(\rho^h \partial_t \mathbf{u}_h) \approx 0$ and likewise $\widetilde{P}(\rho^h \partial_t T_h) \approx 0$.

3.2.2. Time discretization of subscale equations

Any time integration scheme could now be applied to discretize in time the finite element Eqs. (17)–(19), together with Eqs. (29)–(31). As it is discussed in [4] the time integration for the subscales could be one order less accurate than for the finite element equations without affecting the accuracy of the numerical scheme. Considering the backward Euler differencing scheme, the subscale Eqs. (29)–(31) yield

$$\widetilde{p}^{n+1} = \tau_c^{n+1} R_c'^{n+1} \tag{41}$$

$$\widetilde{\mathbf{u}}^{n+1} = \left(\frac{\rho^{h,n+1}}{\Delta t} + \frac{1}{\tau_m^{n+1}}\right)^{-1} \left(\mathbf{R}_m'^{n+1} + \frac{\rho^{h,n}\widetilde{\mathbf{u}}^n}{\Delta t}\right) \tag{42}$$

$$\widetilde{T}^{n+1} = \left(\frac{\rho^{h,n+1} c_p}{\Delta t} + \frac{1}{\tau_e^{n+1}}\right)^{-1} \left(R_e'^{n+1} + \frac{\rho^{h,n} c_p \widetilde{T}^n}{\Delta t}\right) \tag{43}$$

where the superscript n indicates that functions are approximated at time step n, and Δt is the time step size, assumed constant for simplicity. From these expressions, we see that the residual of the momentum and energy equations are multiplied respectively by

$$\tau_{tm} = \left(\frac{\rho^h}{\Delta t} + \frac{1}{\tau_m^{n+1}}\right)^{-1} \tag{44}$$

$$\tau_{te} = \left(\frac{\rho^h c_p}{\Delta t} + \frac{1}{\tau_e^{n+1}}\right)^{-1} \tag{45}$$

These can be considered the effective stabilization parameters for the transient Low Mach equations. Expressions with asymptotic behavior similar to coefficients τ_{tm}, τ_{te} in terms of h, μ, $|\mathbf{u}_h + \widetilde{\mathbf{u}}|$, and Δt can often be found in the literature (see e.g. [14]). It is important to note that if the stabilization parameter depends on Δt and subscales are not considered time dependent, *the steady-state solution will depend on the time step size*. This does not happen if expressions (42) and (43) are used. It can be checked that, when steady state is reached the usual expressions employed for stationary problems are recovered, namely $\widetilde{\mathbf{u}} = \tau_m \mathbf{R}_m$, and $\widetilde{T} = \tau_e R_e$.

The equations for the subscales must be discretized in time as explained and linearized together with the finite element Eqs. (17)–(19). Detailed linearization schemes for these equations are described in [2].

4. Conservation of kinetic energy and dissipative structure

Global conservation statements for mass, momentum and internal energy have been obtained for the present semi-discrete formulation in [2]. In this section we discuss the global conservation of kinetic energy, and the dissipative structure of the formulation. For the continuous problem, kinetic energy conservation is obtained by taking the test function equal to the velocity in the momentum Eq. (8), and using in a crucial manner the mass conservation equation to conclude that the convective terms in the corresponding equations only contribute through boundary terms. Doing this, the kinetic energy conservation for the continuous problem reads

$$c(\rho, \mathbf{u}, \mathbf{u}, \mathbf{u}) - \int_{\partial\Omega} \mathbf{n} \cdot (\mathbf{u} \cdot \mathbf{t}) + \int_\Omega 2\mu \boldsymbol{\varepsilon}' : \boldsymbol{\varepsilon}' = \int_\Omega \mathbf{F} \cdot \mathbf{u} + \int_\Omega p \nabla \cdot \mathbf{u} \tag{46}$$

where $\mathbf{t} = -p\mathbf{I} + 2\mu\boldsymbol{\varepsilon}'(\mathbf{u}_h)$. At the continuous level $c(\rho, \mathbf{u}, \mathbf{u}, \mathbf{u})$, gives the total kinetic energy variation plus the flux of kinetic energy through the boundary using any form of the convective term. The second term is the power of (internal) tractions and the third term is the molecular dissipation (due to viscous effects) These terms are balanced on the right side by the mechanical power of external forces and pressure.

The discrete kinetic energy conservation, obtained taking $\mathbf{v}_h = \mathbf{u}_h$ in the discrete Eq. (18), is

$$c(\rho^h, \mathbf{u}_h + \widetilde{\mathbf{u}}, \mathbf{u}_h, \mathbf{u}_h) - \int_{\partial\Omega} \mathbf{n} \cdot (\mathbf{u}_h \cdot \mathbf{t}_h) + \int_\Omega 2\mu \boldsymbol{\varepsilon}'(\mathbf{u}_h) : \boldsymbol{\varepsilon}'(\mathbf{u}_h) = \int_\Omega \mathbf{F} \cdot \mathbf{u}_h + \int_\Omega p_h \nabla \cdot \mathbf{u}_h - \varepsilon_{\text{num}} \tag{47}$$

where the numerical dissipation ε_{num} is

$$\varepsilon_{\text{num}} = -\sum_K \int_K \widetilde{\mathbf{u}} \cdot \left(\rho^h (\mathbf{u}_h + \widetilde{\mathbf{u}}) \cdot \nabla \mathbf{u}_h + \nabla \cdot (2\mu \boldsymbol{\varepsilon}'(\mathbf{u}_h))\right) - \sum_K \int_K \widetilde{p} \nabla \cdot \mathbf{u}_h + \sum_K \int_K \frac{\partial}{\partial t} (\rho^h \widetilde{\mathbf{u}}) \cdot \mathbf{u}_h \tag{48}$$

where $\mathbf{t}_h = p_h \mathbf{I} - 2\mu\boldsymbol{\varepsilon}'(\mathbf{u}_h)$. The discrete kinetic energy is defined as $k_h = \frac{1}{2}\rho^h \mathbf{u}_h \cdot \mathbf{u}_h$. Note that, unless the numerical dissipation ε_{num}, all other terms in Eq. (47) correspond to the discrete counterpart of the continuous energy balance (46). Through Eqs. (10) and (11) it is seen that $c(\rho^h, \mathbf{u}_h + \widetilde{\mathbf{u}}, \mathbf{u}_h, \mathbf{u}_h)$ gives the total discrete kinetic energy variation plus the flux of kinetic energy through the boundary plus an extra term that depends on the form of the convective term. Only when the skew-symmetric form is used this extra term does not appear, as (13) is also valid in the discrete case for any field **a**. If any the conservative or nonconservative form of the convective term is used, either extra dissipation is being added or, what is worst, subtracted from the system. It is shown in [7] that not using the skew-symmetric form results in the addition of negative dissipation in the case of homogeneous isotropic turbulence, leading in some cases to the blow up of the numerical simulation.

The numerical dissipation ε_{num} contains artificial energy balance terms due to numerical discretization. On the first row, the first term inside the integral can be related to the Cross and Reynolds terms coming from a LES model, accounting for kinetic energy transfer to non resolved scales (until Kolmogorov scale length). The second term inside the integral is only introduced when second or higher order finite elements are implemented. The first term on the second row of (48) is the power done by the pressure subscale, penalizes local mass conservation error and its sign is not known a priori. For incompressible flows this work introduces always positive dissipation, penalizing incompressibility. The second term on the second row of (48) is dissipation due to the subscale variation in time; note that this term vanishes when the DOSS approximation is implemented, due to orthogonality between scale spaces.

An important point for a discrete approximation of the problem is to preserve the dissipative structure defined by the molecular dissipation (third term on left hand side of (46)). More precisely, a classical requirement for LES models introduced by Lilly [15] is that dissipation introduced at the discrete level ε_{num}, should be statistically proportional to the molecular dissipation of the flow, see [10]. For the DOSS method, it is proved in [9] that the dissipation introduced by these extra terms has the same statistical behavior in fully developed incompressible turbulence than for the continuous problem.

5. Numerical results

In this section the performance and accuracy of the developed stabilization methods using dynamic nonlinear subscales are shown for laminar and turbulent flows. The first example is a laminar flow problem where it is compared the performance of the DASGS and DOSS methods, described in Section 3. These methods are compared against the more standard Algebraic SubGrid Scale (ASGS) method [16], in which the subscales are taken as in the DASGS method but neglecting their nonlinear contributions and their time dependency. Similarly, the OSS method is obtained from the DOSS method with the same simplifications. The numerical dissipations introduced by the different formulations are compared and discussed for this laminar case. The second and third problems are the turbulent channel flow and a turbulent thermal driven cavity, respectively, where the ability of the nonlinear subscale method to model turbulence without any physical model is evaluated comparing the obtained results against LES and DNS solutions available in the literature.

5.1. Transient injection flow at low Mach regime

The transient injection flow was proposed in [17] as a test case for low Mach number solvers, and recently considered in [2] using only the DASGS method. It is used here to evaluate the results obtained using the DOSS method. The problem domain is $\Omega = [-L/2, L/2] \times [0, H]$, where $L = 3$ m and $H = 7$ m. The initial values are $T_0 = 300$ K and $p_0^{\text{th}} = 10^5$ Pa, resulting in an initial density of $1.161\ \frac{\text{kg}}{\text{m}^3}$. Furthermore $\mu = 0.005\ \frac{\text{kg}}{\text{m s}}$ and $\text{Pr} = 0.71$ are taken. Zero Dirichlet boundary conditions for the velocity are assumed on all boundaries, except for a small hole in the bottom wall at $[-l/2, l/2]$ where $l = 0.2$ m. Through this hole fluid is injected subject to a parabolic inflow profile $\mathbf{u}_d = (0, 2.5830(1.0 - 100x^2))$ m/s. The temperature of the injected fluid is $T_D = 600$ K. Aside from this, adiabatic boundary conditions are prescribed on all boundaries. We consider a gravity $\mathbf{g} = (0, -9.81)\ \text{m/s}^2$.

The domain is discretized with 60×60 bilinear elements, and the time step size is chosen to be $\Delta t = 0.06$ s. The computation is advanced until $t_{\text{end}} = 6.2$ s using the second order time integration scheme BDF2.

The results obtained with our stabilization method using dynamic subscales in the space of the residuals (DASGS) and when these are orthogonal to the finite element space (DOSS) are compared to those obtained using the ASGS method and a reference solution obtained using a much finer mesh of 17,000 biquadratic elements and 68,541 nodes and a time step of $\Delta t = 0.02$ s. Cuts of temperature and x-velocity fields at $y = 5.6$ m and $x = 0.2$ m when $t = 6.2$ s are depicted in Fig. 1. A gain in accuracy is observed when the method of dynamic and nonlinear subscales is used, specially when using orthogonal subscales. The obtained temperature distribution over $x = 0.2$ m is very different when $y \to 0$, close to the walls. This difference is due to the artificial conduction introduced by the method, which is greater for the ASGS method, lower for the DASGS method, and much lower when using the DOSS method. Note from Fig. 1 (bottom-right) that DOSS results tend to satisfy the adiabatic condition imposed on the wall, wheares ASGS and DASGS do not. In any case, this section is close to the point where the boundary condition for temperature changes from Dirichlet-type to Neumann-type, with the lack of regularity that this implies.

Time evolutions of thermodynamic pressure, velocities and temperature at point $(0.4, 4.0)$ m are compared in Fig. 2. This figure shows a higher temporal accuracy of the scheme when transient nonlinear subscales are used, especially when they are orthogonal (DOSS). It is observed in Fig. 2 that temperature and velocity evolution curves are *advanced in time* when using the ASGS method. This behavior is due to an excessive artificial dissipation of the ASGS formulation. From this reasoning it can be concluded that the DASGS method is less dissipative than the ASGS one, and the DOSS method introduces still less artificial dissipation. Thermodynamic pressure evolution presents much higher accuracy when using the DASGS and the DOSS methods. This is due to global energy conservation property stated in [2], where the conserved internal energy depends only on the thermodynamic pressure p^{th}.

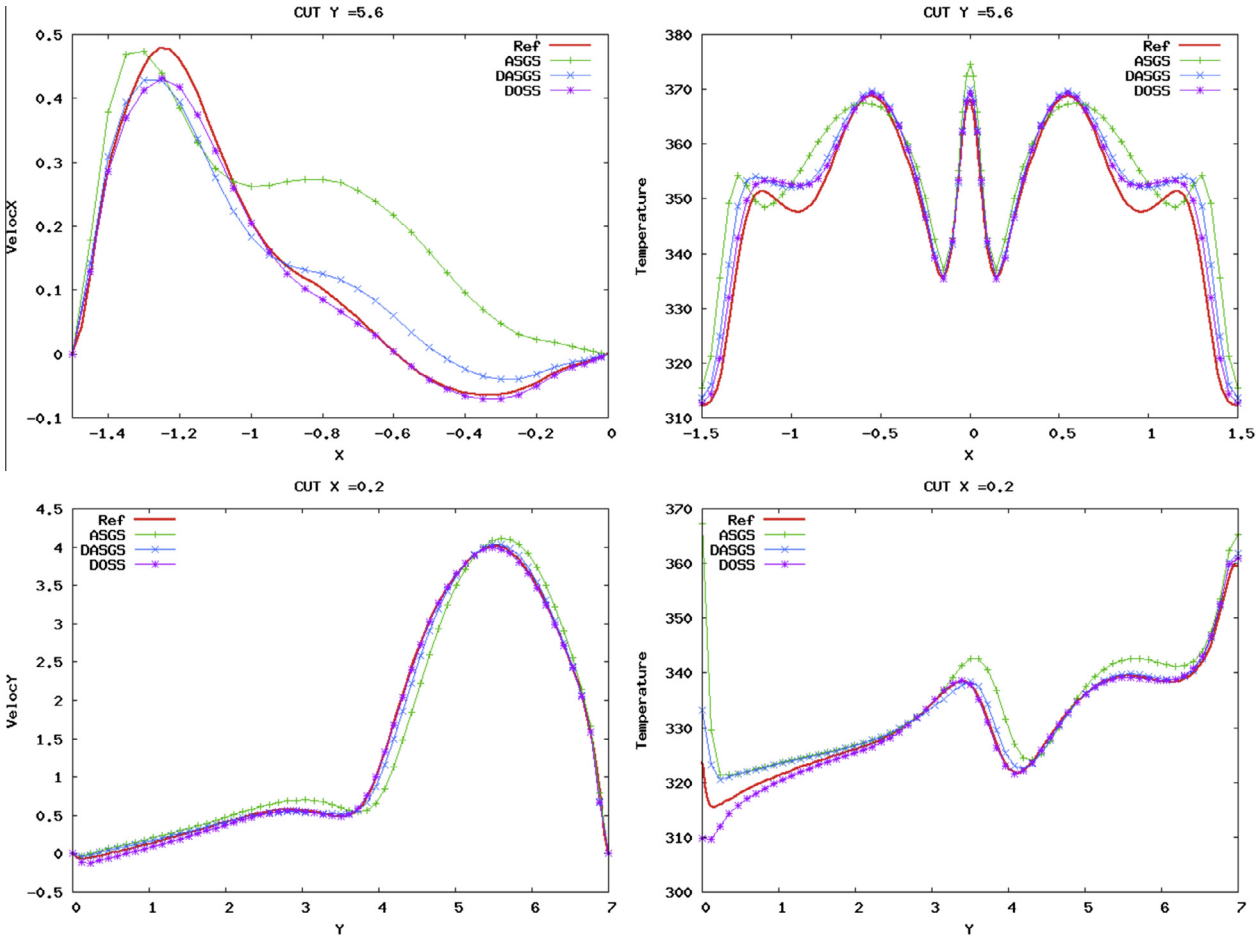

Fig. 1. Cuts of the solution at $y = 5.6$ m and $x = 0.2$ m when $t = 6.2$ s for different stabilization methods against the reference solution.

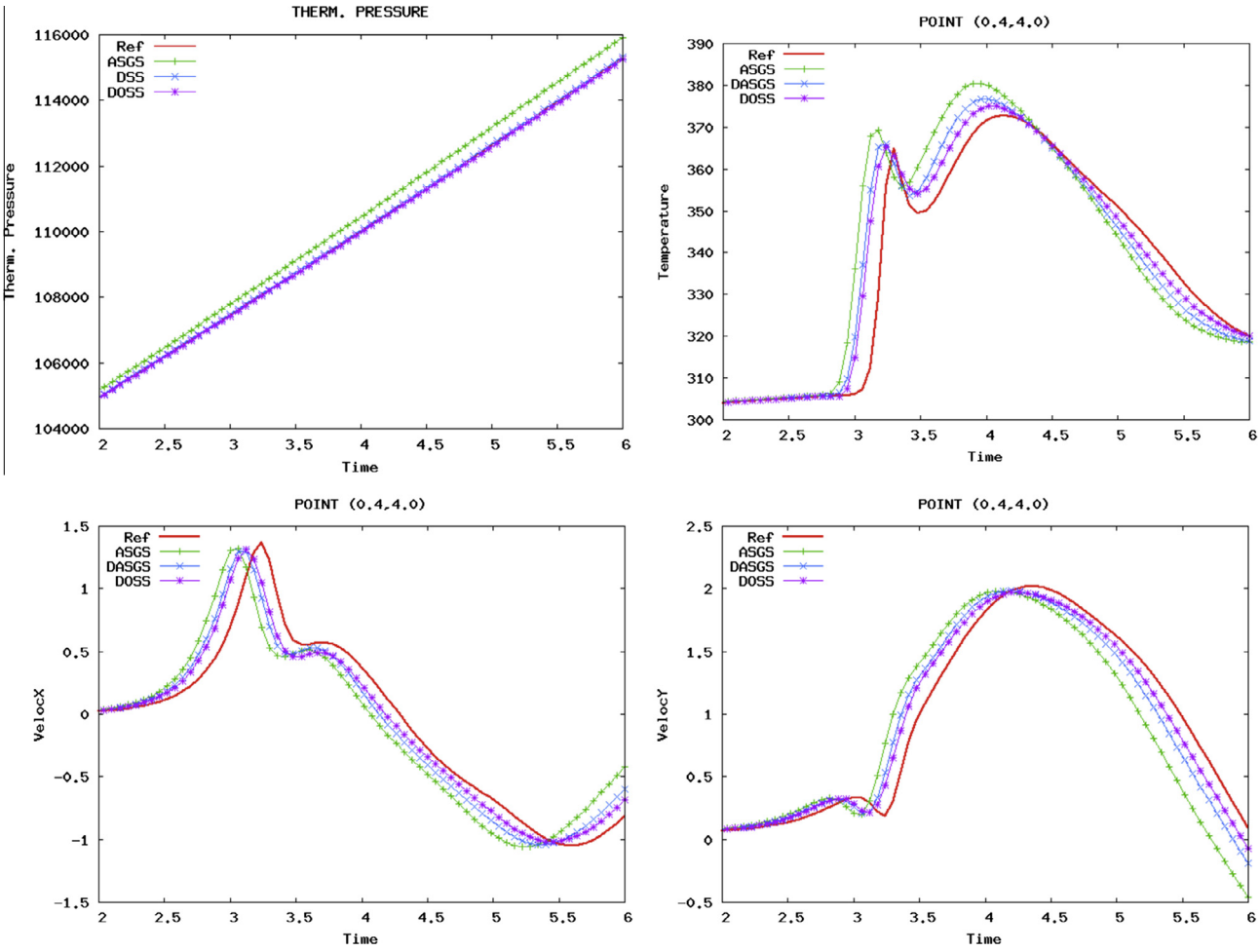

Fig. 2. Point evolution of the unknowns when using the ASGS, the DASGS and the DOSS stabilization methods against the reference solution.

5.2. The turbulent channel flow

5.2.1. Statement of the problem

We next consider a turbulent flow in a channel with two isothermal walls fixed at hot and cold temperatures T_h and T_c. The friction Reynolds number on each wall $\mathrm{Re}_\tau = \frac{\rho u_\tau \delta}{\mu}$ is based on the friction velocity $u_\tau = \sqrt{\tau_w/\rho_w}$, where τ_w is the wall stress

$$\tau_w = \mu \boldsymbol{\varepsilon}'(\mathbf{u}_h)\cdot \mathbf{n} = \mu \partial_y \left(u_x - \frac{2}{3} u_y \right)\Big|_{\text{wall}}$$

δ is the channel half-width and ρ_w the density on the wall. Since ρ, μ and u_τ are variable and different in the hot and cold walls, reference values need to be defined.

The molecular Prandtl number is $\mathrm{Pr} = \frac{c_p \mu}{k} = 0.71$. Two cases with temperature ratios $T_h/T_c = 1.01$ and $T_h/T_c = 2.00$ are investigated. DNS data for this Reynolds number and these temperature ratios T_h/T_c are provided in [18,19], LES results were reported in [20,21,8]. In the case of lower temperature ratio the temperature is almost uniform, offering the opportunity to compare the results to the well-established incompressible DNS data in [22].

As usual in DNS and LES studies of this case, scaled initial temperatures and density fields $T_0 = T_c = 1$ K, $\rho_0 = 1$ kg/m^3 are prescribed. In this way the gas constant and specific heat capacity are assumed to be $R = 287.0$ J kg^{-1} K^{-1} and $c_p = 1004.5$ J kg^{-1} K^{-1}, giving a specific heat ratio $\gamma = \frac{c_p}{c_p - R} = 1.4$. A scaled Sutherland law (4) as used in [18,19,8] is employed, where $T_{\text{ref}} = 1.0$ K and $S = 0.368$ K. The reference density of the problem is $\rho_{\text{ref}} = \rho_0 = 1$ kg/m^3.

Let the coordinate directions x, y and z denote the streamwise, wall-normal and spanwise directions, respectively. The dimensions of the domain are $4\pi\delta \times 2\delta \times \frac{4}{3}\pi\delta$, as in [18]. The walls of the channel are held at zero velocity and constant temperature, the hot wall is at $y = \delta$ and the cold wall at $y = -\delta$. On the other hand, the boundaries of the domain normal to the x and z directions are periodic. Therefore, the total mass of the system is conserved, i.e., this is an example of flow in a closed domain and thermodynamic pressure will be determined at each time step from Eq. (6). The total mass of the system is initially fixed as $m_0 = \int_\Omega \rho_o$. A constant body force $\mathbf{F}$ in the streamwise x-direction, equivalent to a pressure difference, is imposed as the driving mechanism together with periodic conditions also for the pressure. As a consequence, the flow is statistically stationary and homogeneous in the x- and z-directions. Therefore the ensemble mean value of any variable u, denoted by $\bar{u}$, is computed, assuming ergodicity [23], by averaging in time as well as in the homogeneous directions, as usual. The Favre averaging $\hat{u}$ is then computed as $\hat{u} = \frac{\overline{\rho u}}{\bar{\rho}}$. Any fluctuating variable u can be decomposed as $u(t) = \bar{u} + u'(t) = \hat{u} + u''(t)$ where, u' and u'' are the Reynolds and Favre fluctuations of u, being by definition $\overline{u'} = 0$ and $\widehat{u''} = 0$.

Three different meshes of 32^3, 48^3 and 64^3 Q_1 finite elements are employed. The distribution of the nodes is uniform in streamwise and spanwise directions x, z. In wall normal direction y the distribution of nodes obeys an hyperbolic tangent function refining

Table 1
Nondimensional mesh element length for the different discretizations.

Mesh	$\Delta y^+_{\min}$	$\Delta y^+_{\max}$	Δx^+	Δz^+
32^3	1.56	24	70	24
48^3	1.01	16	47	16
64^3	0.76	12	35	12

node spacing towards the wall, as in [18,8]. For the case of low temperature ratio a symmetric node distribution between the lower and the upper walls is used. The location y^i of each grid node i, $i = 0, \ldots, n_y$, where n_y is the number of elements in the wall normal direction, is given by

$$y^i = \frac{\tanh\left(2.1\left(\frac{2i}{n_y} - 1\right)\right)}{\tanh(2.1)}$$

In Table 1 the main discretization lengths in wall units for the different meshes are provided.

For the high temperature ratio the Reynolds number near the hot wall is expected to be smaller than near the cold wall and the following non-symmetric distribution is used:

$$y^i = 2\frac{\hat{y}^i + 1}{\hat{y}^{n_y+1}} - 1$$

with

$$\hat{y}^i = \frac{\tanh\left(2.1\left(\frac{2\alpha i}{n_y} - 1\right)\right)}{\tanh(2.1)}$$

and $\alpha = 0.9$.

The equations are integrated in time using a second order scheme (BDF2) and a constant time step $\Delta t = 0.004$s which expressed in wall units is $\Delta t^+ = \frac{\Delta t}{\Delta t^*} = \frac{\Delta t \rho u_\tau^2}{\mu} = 0.72$. Following [8], at least 5000 time steps are performed to allow the flow to develop and reach a statistically steady state. The statistics are collected during 5000 more time steps, a time period of order $T \approx 15\delta/u_{\tau,\mathrm{m}}$, where $u_{\tau,\mathrm{m}} = (u_{\tau h} + u_{\tau c})/2$ is the mean friction velocity, $u_{\tau h}$ and $u_{\tau c}$ being the friction velocities of the hot and cold walls, respectively.

Due to the difference in densities and viscosities the hot and cold walls have different friction Reynolds numbers. A friction Reynolds number needs to be defined in order to characterize the channel flow problem as a whole. Let us define this bulk friction Reynolds number as $\overline{\mathrm{Re}}_\tau = \frac{\rho_{\mathrm{ref}} \overline{u}_\tau \delta}{\mu_{\mathrm{ref}}}$, where $\overline{u}_\tau = \sqrt{\frac{\tau_{w,\mathrm{m}}}{\rho_{\mathrm{ref}}}}$ is the reference friction velocity based on the average of wall stresses, $\tau_{w,\mathrm{m}} = (\tau_{wc} + \tau_{wh})/2$, and μ_{ref} is the reference viscosity corresponding to temperature T_{ref}. Applying global momentum balance over the entire channel, assuming statistically steady state, we get the following relationship between the driving force in the streamwise direction F_x and the wall stress:

$$F_x \delta = \tau_{w,\mathrm{m}} = \rho_{\mathrm{ref}} \overline{u}_\tau^2$$

Making use of this relationship, the friction Reynolds number is expressed in terms of the driving force as

$$\overline{\mathrm{Re}}_\tau = \frac{\sqrt{\mathrm{F_x} \rho_{\mathrm{ref}} \delta^3}}{\mu_{\mathrm{ref}}}$$

The problem is defined by $\overline{\mathrm{Re}}_\tau = 180$ which is obtained fixing the driving force to $F_x = 1$ N/m, and the reference viscosity to $\mu_{\mathrm{ref}} = \frac{1}{180}$ kg m^{-1} s^{-1}.

5.2.2. Numerical results

As it is shown in [2] and in the previous example, the present DASGS and DOSS methods are less dissipative and more accurate than the ASGS method, at least for laminar flows. Nevertheless, excellent results have been obtained recently in Trofimova et al. [24], for the turbulent channel flow using only ASGS stabilization without any turbulence model, tuning the stabilization parameter in order to add the smallest possible amount of numerical dissipation. The obtained results were also better than those obtained using advanced LES models over the same mesh.

As a general trend in the present example, we have observed in our numerical model that the results improve when less numerical dissipation is introduced (comparing to DNS given by Moser et al. [22]), provided of course that numerical stability is kept. We have also observed that the numerical dissipation comes mainly from cross dissipation and from the work of the pressure subscale terms. As will be shown below (see Fig. 13) those terms are dominant respect to all other dissipative terms in Eq. (48). Numerical dissipation depends on the value of the subgrid components $\widetilde{\mathbf{u}}$ and $\widetilde{p}$. Due to the highly anisotropic shape of the elements, we have found crucial to define h in (32)–(34) as the element length in the y-direction, being the minimum element length in almost all domain. In this way lower values for τ_m and τ_c are obtained, and therefore the introduced amount of numerical dissipation is lower. As the mesh is non uniform, the obtained y-distribution of the stabilization parameters τ_c, τ_m and τ_e are discontinuous and highly oscillatory element by element. We have observed that to smooth the stabilization parameters improves the obtained results. The results that we show in this section have been obtained taking h as explained and smoothing the obtained stabilization parameters. This smoothing is done by projecting the mesh size h over the finite element space, obtaining a continuous distribution of h and then smoothed stabilization parameters.

We have tried to solve the present problem using ASGS stabilization only, finding that the stabilization parameters τ_m, τ_e need to depend on time step size Δt to obtain a stable calculation. Otherwise the nonlinear system of equations is unable to converge. This is in accordance with the observations in [7], where the analysis of the different VMS methods (i.e. OSS and ASGS, static and dynamic, linear and non-linear) in the small time step limit is performed for the present problem. To consider τ_m and τ_e depending on Δt and to consider the subscales not time dependent is inconsistent, because the steady-state solution (in case of being reached) would depend on the time step size [4]. If $\Delta t \to 0$, stabilization would be lost.

A snapshot of the velocity and temperature distribution inside the channel when $T_H/T_C = 2$ is shown in Fig. 3, with the only

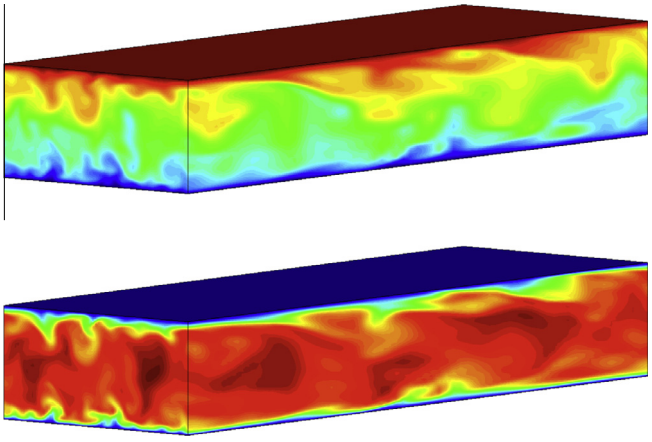

Fig. 3. Snapshot of temperature (top) and velocity (bottom) distribution inside the turbulent channel for the case $T_H/T_C = 2$.

purpose of having a general view of the flow. The flow and heat transfer parameters of interest for both heat transfer cases are listed in Tables 2 and 3 against DNS data. The friction Reynolds number at the cold and hot walls are denoted as $\mathrm{Re}_{\tau c}$ and $\mathrm{Re}_{\tau h}$, respectively, and are compared against the values obtained by Nicoud and Poinsot in [25] for the nearly incompressible case, and against the values obtained by Nicoud in [19] for the higher temperature ratio case.

For the nearly incompressible case the tabulated values are on the cold wall, and are compared against the DNS data from [25]. The obtained Nusselt numbers are compared to DNS values referred in [21]. For the case $T_H/T_C = 2$ the tabulated values are compared to the DNS data also from [25].

Since there are differences in the literature, let us define the way to compute dimensionless parameters that we have used. The bulk Reynolds number in Tables 1 and 2 is defined as

$$\mathrm{Re}_b = \frac{\rho_m U_m \delta}{\mu_m} \tag{49}$$

where

$$\rho_m = \frac{1}{2\delta}\int_{-\delta}^{+\delta} \bar{\rho}\, dy, \quad U_m = \frac{1}{2\delta\rho_m}\int_{-\delta}^{+\delta} \bar{\rho}\hat{u}_x\, dy$$

and the bulk viscosity μ_m is evaluated at the bulk temperature T_m, defined as

$$T_m = \frac{1}{2\delta\rho_m U_m}\int_{-\delta}^{+\delta} \bar{\rho}\widehat{u_x T}\, dy$$

The Nusselt number is defined

$$\mathrm{Nu} = \frac{4}{T_m^+}\left.\frac{\partial T^+}{\partial y}\right|_w$$

where

$$T_m^+ = \frac{|T_w - T_m|}{T_\tau}$$

and the subscript w indicates that the property is evaluated on the wall, either the cold or the hot one. The friction temperature T_τ and the wall heat flux q_w are respectively

$$T_\tau = q_w/(\rho_w c_p u_\tau), \quad q_w = \left|k_w \frac{\partial T_w}{\partial n}\right|$$

and $T^+ = \frac{|T-T_w|}{T_\tau}$ is a dimensionless temperature scaled by the friction temperature. Finally, the heat flux wall parameter B_q is

$$B_q = \frac{q_w}{\rho_w c_p u_{\tau w} T_w}$$

The friction factor at the wall C_f is based on the mean density on the channel ρ_m and the maximum velocity $U_{\max}$, being defined as

$$C_f = \frac{2\tau_w}{\rho_m U_{\max}^2}$$

For both cases the bulk Reynolds numbers are larger than DNS data. These averaged quantities are very similar for the DASGS and DOSS methods.

For the high temperature ratio problem $T_H/T_C = 2$, Nicoud [19] found Reynolds values of $\mathrm{Re}_{\tau c} = 200$ and $\mathrm{Re}_{\tau h} = 82$ over cold and hot walls, differing a little from those obtained in the present work. In [20] the values obtained are respectively 224.1 and 91.2, much closer to those that we have obtained. The strategy adopted in this reference is to take as initial condition the solution corresponding to the lower temperature ratio at a time where the flow is fully developed, which is the same strategy that we have used here. The friction values are very sensitive to the conductivity values over the wall, leading to some differences in the obtained solutions between Nicoud in [19] and the present work for the case $T_H/T_C = 2.0$. The friction Reynolds number over the hot wall $\mathrm{Re}_{\tau h} \approx 93$ is too low to maintain full turbulence, therefore the solution could reflect low-Reynolds number effects. For greater temperature ratios T_H/T_C the Reynolds number over the hot wall is expected to be smaller. To circumvent this low Reynolds number behavior some authors assume that viscosity and thermal conductivity decrease with temperature as $\mu,\ k \propto 1/\sqrt{T}$ [25], being this kind of behavior relevant to a liquid. Assuming this temperature dependence the friction Reynolds number over the hot wall is not too small in comparison with the value over the cold wall, the problem exhibits a more symmetric solution, and permits the use of a symmetric mesh.

Fig. 4 on the left depicts mass flow rate per unit area across the channel. It is seen that for the case $T_H/T_C = 1.01$ the mass flow is nearly symmetric since the density is nearly constant, whereas for the case $T_H/T_C = 2$ the mass flow on the cold wall side is considerably larger than that on the hot wall side due to density variation across the channel. The right of Fig. 4 depicts mean velocity across the channel for cases $T_H/T_C = 1.01$ and $T_H/T_C = 2$. For the high ratio case $T_H/T_C = 2$ the velocity profile does not deviate much from the low hot/cold case $T_H/T_C = 1.01$. But as will be shown shortly, the deviations are nevertheless quite significant when plotted in wall coordinates y^+. Upon a closer examination, it is found that the slope of the velocity profile is steeper on the cold side ($y \to -1$) than on the hot side ($y \to +1$). Considering that a uniform heat flux Q_h satisfies the energy conservation Eq. (19),

Table 2
Mean flow and heat transfer parameters for the channel flow when $T_H/T_C = 1.01$. The number of elements per direction is indicated in the mesh-method definition.

Mesh-method	$\mathrm{Re}_{\tau c}$	$\mathrm{Re}_{\tau h}$	Re_b	$10^3 C_f$	Nu
32DASGS	182	178	3378	4.4	22.6
48DASGS	181	178	3143	5.0	23.6
64DASGS	182	179	3034	5.4	24.4
32DOSS	182	178	3405	4.3	22.5
48DOSS	180	180	3138	5.0	23.2
64DOSS	180	179	3042	5.3	23.8
DNS	185	182	2855	6.1	21.0

Table 3
Mean flow and heat transfer parameters for the channel flow $T_H/T_C = 2$. (h): hot wall, (c): cold wall. The number of elements per direction is indicated in the mesh-method definition.

Mesh-method	$\mathrm{Re}_{\tau c}$	$\mathrm{Re}_{\tau h}$	Re_b	$10^3 C_f(c)$	$10^3 C_f(h)$	$10^2 B_q(c)$	$10^2 B_q(h)$	$\mathrm{Nu}(c)$	$\mathrm{Nu}(h)$
32DASGS	219	93	2406	4.7	4.5	1.82	1.29	23.4	13.1
48DASGS	220	93	2247	5.3	5.1	1.91	1.36	24.6	13.9
64DASGS	222	93	2169	5.8	5.5	1.99	1.36	26.2	13.9
32DOSS	219	93	2359	4.8	4.7	1.82	1.30	23.3	13.4
48DOSS	221	91	2247	5.5	5.0	1.89	1.34	25.3	13.1
64DOSS	221	93	2160	5.8	5.6	1.96	1.38	25.6	14.0
DNS	200	82	1786	6.5	5.6	1.8	1.4	N A	N A

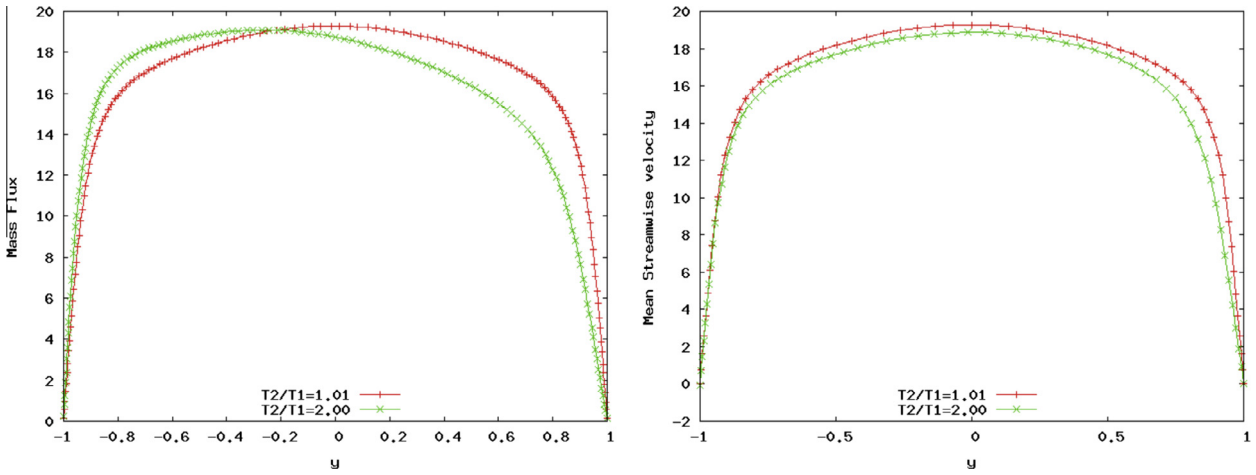

Fig. 4. Mean profile of velocity (right) and mass flux ρu_x across the channel (left) for cases $T_H/T_C = 1.01$ and $T_H/T_C = 2$. Mesh of 64^3 elements and DASGS method.

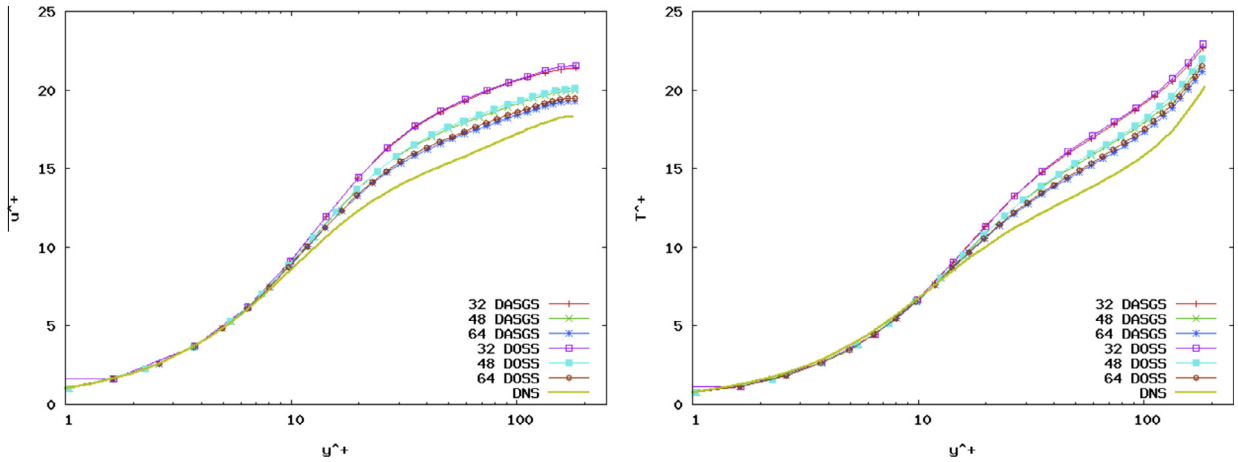

Fig. 5. Mean profile of velocity (left) and temperature (right) for the case $T_H/T_C = 1.01$ using the DASGS and DOSS methods. The number of elements per direction is indicated in the legends.

the wall heat flux must be the same through the hot and cold walls, i.e., $\overline{k\partial_y T_h}|_h = \overline{k\partial_y T_h}|_c$. Therefore, temperature profiles will be steeper close to the cold wall due to Sutherland's law.

Fig. 5 depicts mean streamwise velocity profiles for the case $T_H/T_C = 1.01$, scaled by the wall shear stress velocity, $u^+ = \frac{u}{u_\tau}$ for the three meshes using the DASGS and DOSS methods. Results are compared against DNS data for incompressible flow, given in [22]. In Fig. 5 the mean temperature profiles scaled by wall temperature, $T^+ = \frac{|T-T_w|}{T_\tau}$, where $T_\tau = q_w/(\rho_w c_p u_\tau)$ and $q_w = -k_w \frac{\partial T_w}{\partial n}$, for the case $T_H/T_C = 1.01$ over the three meshes are also shown.

At this point, a remark is needed concerning the implementation of the DOSS method. For linear elements, we usually perform the projection using a nodal quadrature rule, resulting in a diagonal matrix. Thus, the projection is trivial to compute. However, if this integration rule is not used in the evaluation of the residual, property $\widetilde{P}(\rho^h \frac{\partial}{\partial t}\mathbf{u}_h) \approx 0$ is deteriorated because of the different way to evaluate integrals. Therefore, we have kept $\rho^h \frac{\partial}{\partial t}\mathbf{u}_h$ in the residual for the results shown in this section. We have found that this term has a very small influence in laminar cases, but affects the evaluation of time averages in turbulent cases because of the correlation between $\widetilde{\mathbf{u}}$ and the convective term in the cross dissipation term in (48) if the temporal derivative is not included in the evaluation of $\widetilde{\mathbf{u}}$. The same comments would apply to the energy equation.

We have also observed that setting $c_1 = 12$ in (32)–(34) instead of setting $c_1 = 4$ as in [2] improves significantly the obtained mean values and fluctuations of the unknowns (being closer to DNS data). As explained in Section 3, this is because fixing $c_1 = 12$ lowers the value of τ_c, reducing the numerical dissipation introduced by the pressure subscale in (48). Again, this findings are in line with the observations made in [7] for incompressible flows. It is worth noting that setting $c_1 = 12$ gives the exact asymptotic value for the advection diffusion equation using one-dimensional uniform meshes.

Root-mean-square values of streamwise, spanwise and wall normal velocities are shown in Fig. 6 for the case $T_H/T_C = 1.01$ compared against DNS data from [22]. The obtained results overpredict velocity fluctuation in the streamwise direction, but under-predict fluctuation in the wall-normal and spanwise directions. Root-mean-square values of temperature are shown in Fig. 6 for the case $T_H/T_C = 1.01$, comparing them to DNS data. It is observed that temperature fluctuation is over-predicted. As the case is nearly incompressible, all results have been shown only for the cold wall. Results for the hot wall are in agreement with the ones for the cold wall with differences lower than 1%.

For the higher temperature ratio case $T_H/T_C = 2$, the obtained mean and RMS profiles are compared to those obtained in [8] using what the authors call Algebraic Variational Multiscale-Multigrid method (AVM^3) over a mesh of 64^3 elements. This method is

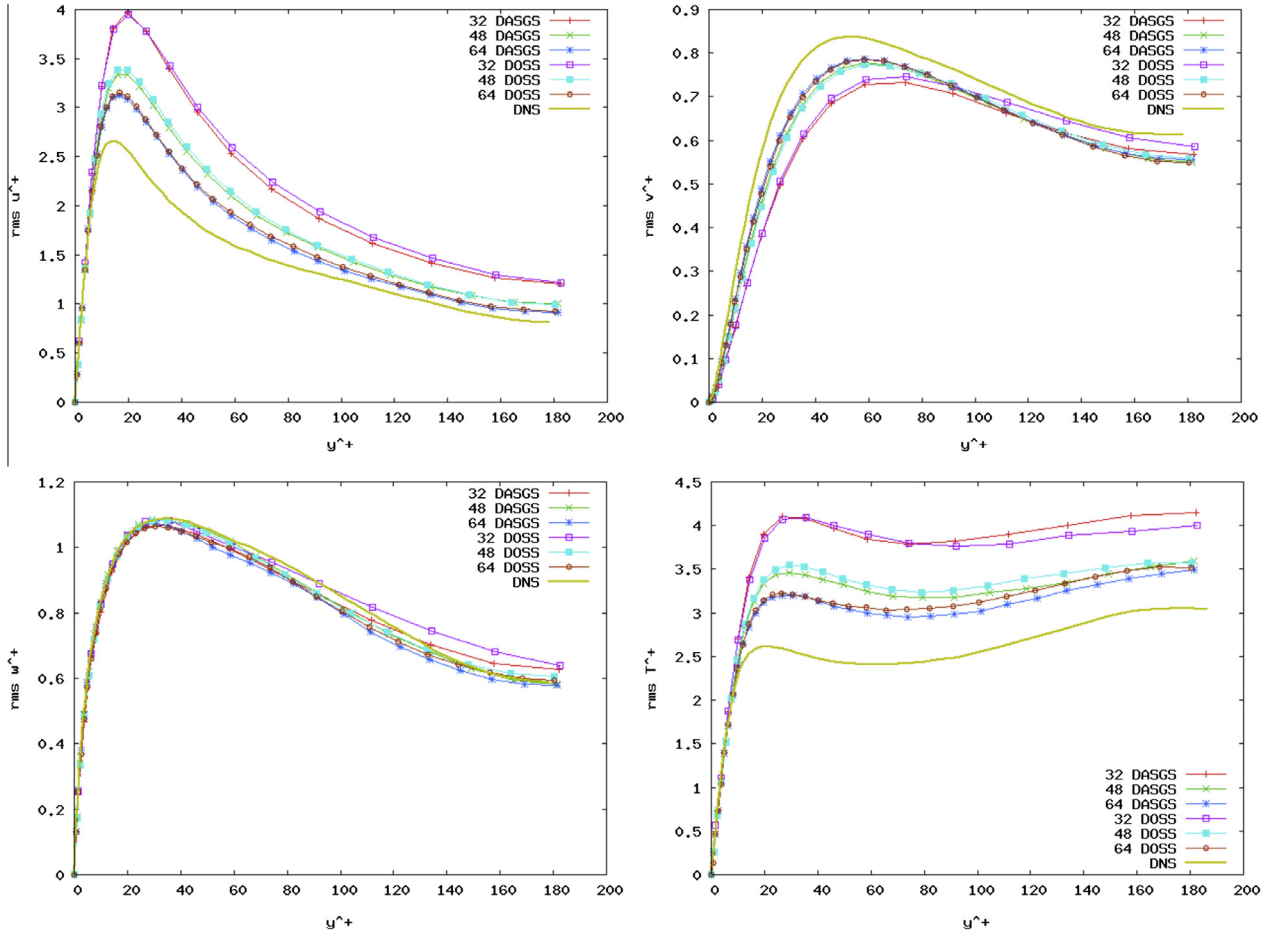

Fig. 6. Velocity and temperature fluctuations for case the $T_H/T_C = 1.01$ using DASGS and DOSS methods. The number of elements per direction is indicated in the legends.

labeled in the figures as '64 AVM^3' corresponding to the method labeled as 'AVMSUP' in [8], being the most accurate method of the different combinations proposed in this reference.

Figs. 7 and 8 show the mean streamwise velocity and mean temperature results for the higher temperature ratio $T_H/T_C = 2$, comparing them to DNS data. It is observed that the results predicted by the DOSS method are slightly better over the coarsest mesh for the hot wall. The velocity profiles obtained using the AVM^3 method [8] are very similar to those obtained using the DOSS and the DASGS methods. However, the temperature profiles obtained over the hot half channel deviate from those obtained using the AVM^3 method. The temperature difference is strong enough to induce a significant asymmetry in the mean quantities.

Root-mean-square values of streamwise, spanwise and wall normal velocities are shown in Fig. 9. Root-mean-square values of temperature are shown in Fig. 10. The predictions of the DASGS and DOSS methods are very similar. However DOSS method gives more accurate results for the cold wall over 32^3 and 48^3 meshes. The RMS velocity profiles obtained in [8] using AVM^3 coincide with those obtained here close to the walls. However, away from the

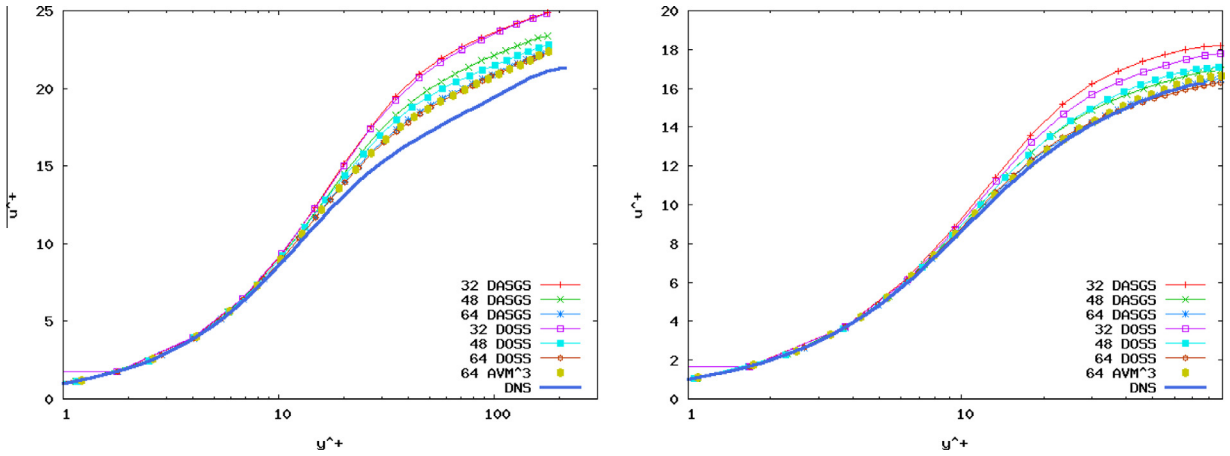

Fig. 7. Mean profile of velocity for the case $T_H/T_C = 2$ using the DASGS and DOSS methods against DNS (left: Cold wall, right: Hot wall).

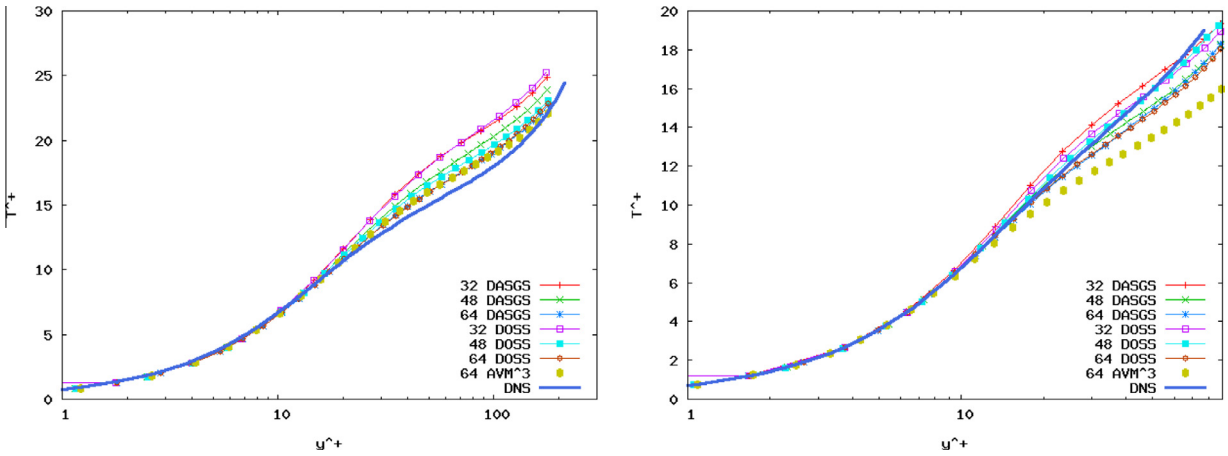

Fig. 8. Mean profile of temperature for the case $T_H/T_C = 2$ using the DASGS and DOSS methods (left: Cold wall, right: Hot wall).

walls the AVM^3 results show more deviation from DNS data than the results obtained by the methods proposed in the present work.

The shear stress distribution across the channel is illustrated in Fig. 11 using the coarsest mesh of 32^3 elements and both heat transfer cases. The *shear stress* τ_h is expressed as

$$\tau_h = \bar{\rho}^h \widehat{u''_{hy} u''_{hx}} - \overline{\mu \partial_y u_{hx}} + \bar{\rho}^h \left(\widehat{u''_{hy} \tilde{u}''_x} + \widehat{\tilde{u}''_y u''_{hx}} + \widehat{\tilde{u}''_y \tilde{u}''_x} \right) \tag{50}$$

The three terms composing τ_h are identified respectively as the resolvable Reynolds shear stress (like in a LES model), the viscous shear stress and the modeled SGS shear stress. The modeled SGS shear stress depends on the subscales, and can be identified with the modeled SGS shear stress $\overline{\mu_{\text{tur}} \partial_y u_x}$ when using LES models, μ_{tur} being the turbulent viscosity (see for example [21]). It is seen that in both heat transfer cases the contribution of the modeled shear stress is very small. This finding is in qualitative agreement with [21] at a similar Reynolds number. The total shear stress distribution is linear, implying that forces are in equilibrium, statistically steady state has been reached and the flow is fully developed. Using finer grids similar distributions were obtained for the shear stress, with the advantage that less time steps were needed to obtain a linear distribution of the total shear stress. High oscillatory distributions of the total shear stress are observed close to the walls which is due to the addition of the element by element discontinuous function $\overline{\mu \partial_y u_{hx}}$ and the continuous function $\overline{\rho^h} \widehat{u''_{hy} u''_{hx}}$, both with the strong variation showed in the figure. Lower oscillations were found when finer grids were used.

Fig. 12 presents the normal heat flux distribution across the channel for both temperature ratio cases using the coarser mesh of 32^3 elements. The total averaged normal heat flux Q_n is

$$Q_n = c_p \overline{\rho^h} \widehat{u''_{hy} T''_h} - \overline{k \partial_y T_h} + c_p \overline{\rho^h} \left(\widehat{u''_{hy} \tilde{T}''} + \widehat{\tilde{u}''_y T''_h} + \widehat{\tilde{u}''_y \tilde{T}''} \right)$$

The three terms composing Q_n represent respectively the resolvable turbulent heat flux, the heat conduction, and the modeled SGS heat flux. As for the shear stress distribution, it is observed that the modeled SGS heat flux is very small. Whereas results for the lower heat transfer case are nearly symmetric with respect to channel centerline, a shift of both heat conduction and resolvable turbulent heat flux distributions towards the cold wall is observed for the higher temperature ratio case, due to its higher Reynolds number and the steeper boundary layer. Note that the total heat flux is constant along the channel as a consequence of the flow being fully developed. Similar distributions were obtained when using finer grids. We have observed that less time steps were needed when using finer grids to obtain a uniform distribution of the total heat flux. We have also observed that more time steps were needed to reach the statistically steady case for the high heat transfer case $T_H/T_C = 2$.

Fig. 13 depicts numerical dissipation distribution along the channel for the case $T_H/T_C = 1.01$ using the coarse mesh of 32^3 elements. There, the distributions of cross and Reynolds numerical stresses, the work of mechanical pressure and the work of pressure subscale are shown. The cross stress and the work of pressure subscales are dominant over all the other terms. The Reynolds stress term $\left(-\sum_K \int_K \tilde{\mathbf{u}} \cdot \rho^h \tilde{\mathbf{u}} \cdot \nabla \mathbf{u}_h\right)$ is very low because it depends on the square of the velocity subscale. This velocity subscale is much lower than the finite element component over all the domain, except very close to the walls where all dissipations are very low. The dissipation introduced by the pressure subscale is higher than the dissipation introduced by the mechanical pressure, because the pressure subscale $\tilde{p}$ is highly correlated with the velocity divergence, whose mean value tends to zero in the nearly incompressible case $T_H/T_C = 1.01$.

On the right of Fig. 13 the distributions of cross and pressure subscale dissipations when setting the numerical parameters $c_1 = 4$ and $c_1 = 12$ are compared. As explained in Section 3, the obtained cross dissipation is insensitive to the c_1 value, obtaining very similar distributions. However, the pressure subscale dissipation is much lower when setting $c_1 = 12$, as discussed in Section 3, and a less dissipative scheme is obtained when $c_1 = 12$ than when $c_1 = 4$. In Fig. 14 the obtained dimensionless mean streamwise velocities and its root-mean-square values when setting $c_1 = 4$ and $c_1 = 12$ are compared against DNS values. It is observed than the obtained solutions using $c_1 = 12$ are closer to DNS value than those obtained when setting $c_1 = 4$.

In Fig. 15 the numerical dissipations introduced by DASGS and DOSS methods are compared, finding that the cross and pressure subscale dissipaton are very similar for both methods. As it was shown in the previous Example 5.1 for laminar problems, the DOSS method introduces less numerical diffusion than the DASGS method. However, this is not the observed behavior in the present turbulent flow, due to correlation in time between variables in the dissipative terms. The averaged numerical dissipation $\bar{\varepsilon}_{\text{num}}$, obtained from (48) can be approximated keeping only the most signigicant terms as

$$\begin{aligned} \bar{\varepsilon}_{\text{num}} &\approx -\sum_K \int_K \overline{\tilde{\mathbf{u}} \cdot (\rho^h \mathbf{u}_h \cdot \nabla \mathbf{u}_h)} - \sum_K \int_K \overline{\tilde{p} \nabla \cdot \mathbf{u}_h} \\ &= -\sum_K \int_K \overline{\tilde{\mathbf{u}}} \cdot \overline{\rho^h \mathbf{u}_h \cdot \nabla \mathbf{u}_h} - \sum_K \int_K \overline{\tilde{p}} \nabla \cdot \overline{\mathbf{u}_h} \\ &\quad - \sum_K \int_K \overline{\tilde{\mathbf{u}}' \cdot (\rho^h \mathbf{u}_h \cdot \nabla \mathbf{u}_h)'} - \sum_K \int_K \overline{\tilde{p}' \nabla \cdot \mathbf{u}'_h} \end{aligned} \tag{51}$$

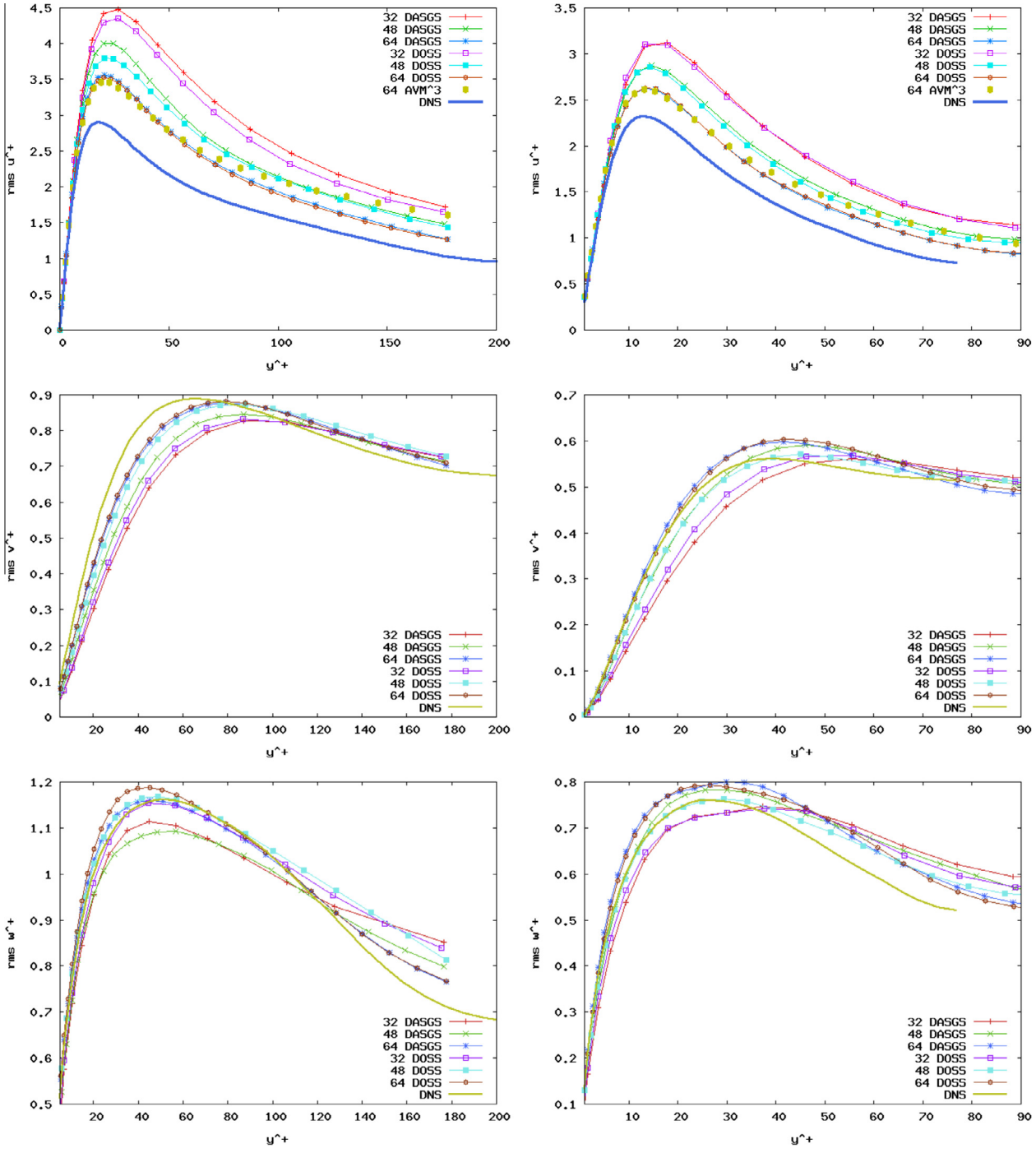

Fig. 9. Velocity fluctuations for the case $T_H/T_C = 2$ using the DASGS and DOSS methods (left: Cold wall, right: Hot wall).

where it is seen that numerical dissipation depends on subscale values of $\widetilde{\mathbf{u}}$ and $\widetilde{p}$, but also on their correlation with the convective and divergence terms $\rho^h \mathbf{u}_h \cdot \nabla \mathbf{u}_h$ and $\nabla \cdot \mathbf{u}_h$, respectively. The averaged subscale values are showed on the right of Fig. 15, where it is seen that DOSS method gives smaller values close to the walls, due to the orthogonal projection. The contribution of fluctuating terms in (51) seems to be important to the numerical dissipation, and larger for the DOSS method.

From numerical experiments we have found that results are quite sensitive to the parameter τ_c in Eq. (32). It was shown in [26] that for incompressible flows condition $c_1 \rho^h \tau_c \tau_m \leqslant h^2$ is required in the heuristic derivation of method. In fact, we have observed numerically than when this condition does not hold the solution deteriorates close to the walls. This happens because when $|\mathbf{u}_h + \widetilde{\mathbf{u}}| \to 0$ the viscous term in the Navier Stokes equations is dominant, the pressure subscale plays an important role and $\tau_c \to \frac{\mu}{\rho^h}$ if $c_1 \rho^h \tau_c \tau_m = h^2$, which is a physically meaningful bulk viscosity.

5.3. Thermal driven cavity with aspect ratio 4

5.3.1. Statement of the problem

The present turbulent example consists in a differentially heated cavity of aspect ratio 4 with adiabatic horizontal walls. This problem has been solved by Trias et al. [27–29] using DNS, and by Ghaisas et al. [30] using LES models. Both groups used the Bous-

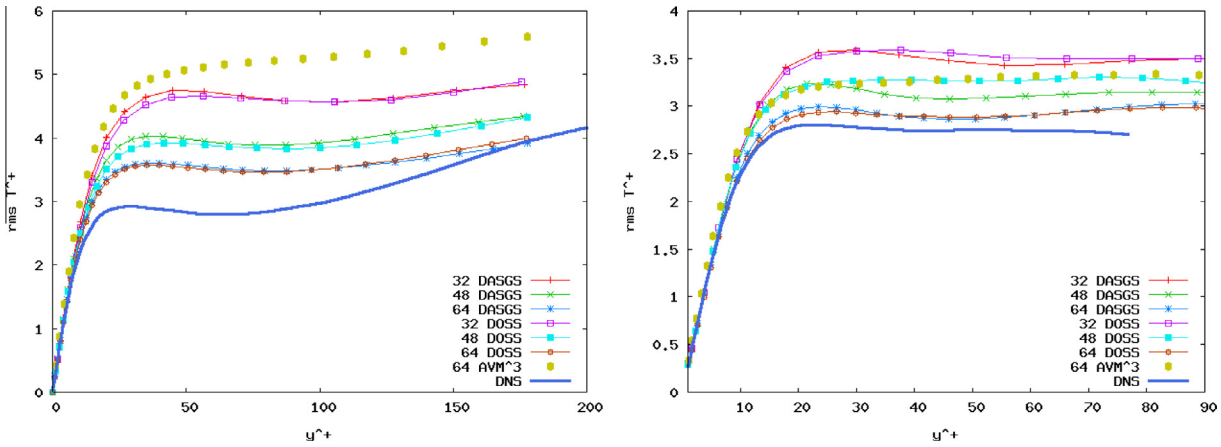

Fig. 10. Root mean square of temperature and Correlation of velocity and temperature fluctuations for the case $T_H/T_C = 2$ using the DASGS and DOSS methods (left: Cold wall, right: Hot wall).

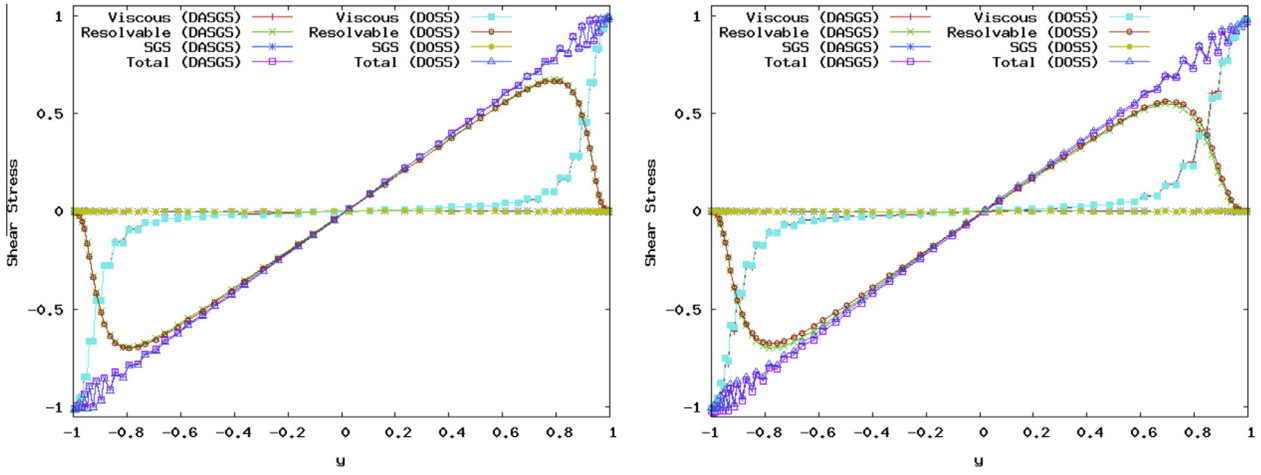

Fig. 11. Shear stress distribution across the channel (scaled by the mean pressure gradient F_x) for cases $T_H/T_C = 1.01$ (left) and $T_H/T_C = 2$ (right) using the DASGS and DOSS methods over the coarsest grid of 32^3 elements.

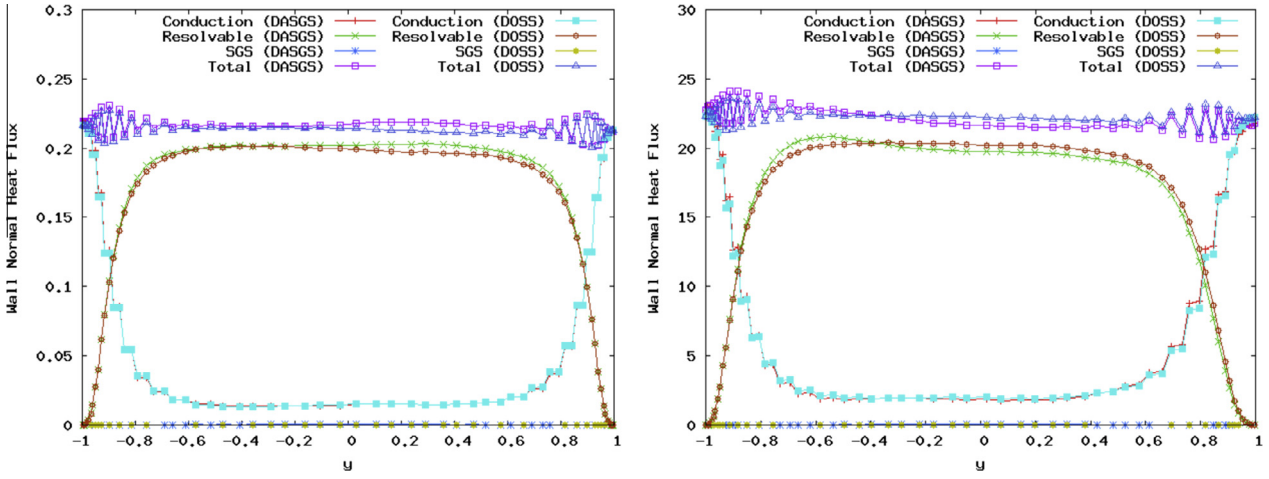

Fig. 12. Thermal energy balance across the channel for cases $T_H/T_C = 1.01$ (left) and $T_H/T_C = 2$ (right) using the DASGS and DOSS methods over the coarsest grid of 32^3 elements.

sinesq approximation to solve the present problem. An scheme of the 3D cavity is shown in Fig. 16. The problem domain is $\Omega = [0, L_x] \times [0, L_y] \times [0, L_z]$ with $L_x = L_z = 1$ m, and $L_y = 0.25$ m. The gravity force **g** points in $-z$ direction. Two vertical walls are maintained at a fixed hot temperature T_H ($y = 0$) and cold temperature T_C ($y = L_y$), adiabatic boundary conditions are prescribed for

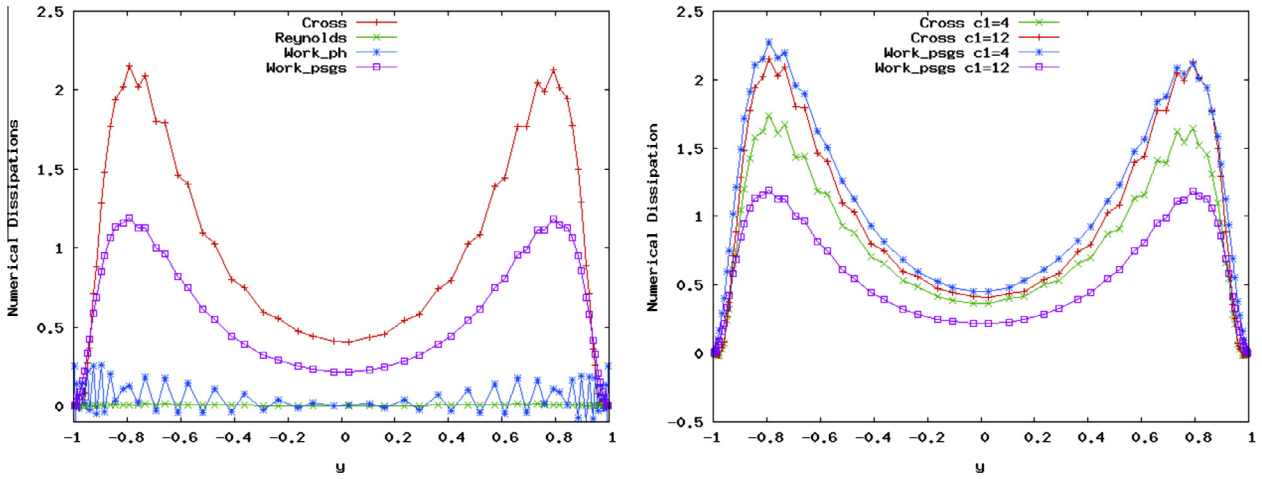

Fig. 13. Numerical dissipation components along the channel (left), and comparison of cross dissipation and work of subscale pressure using $c_1 = 4$ and $c_1 = 12$ (right) for the case $T_H/T_C = 1.01$ using the DASGS method over the coarsest grid of 32^3 elements.

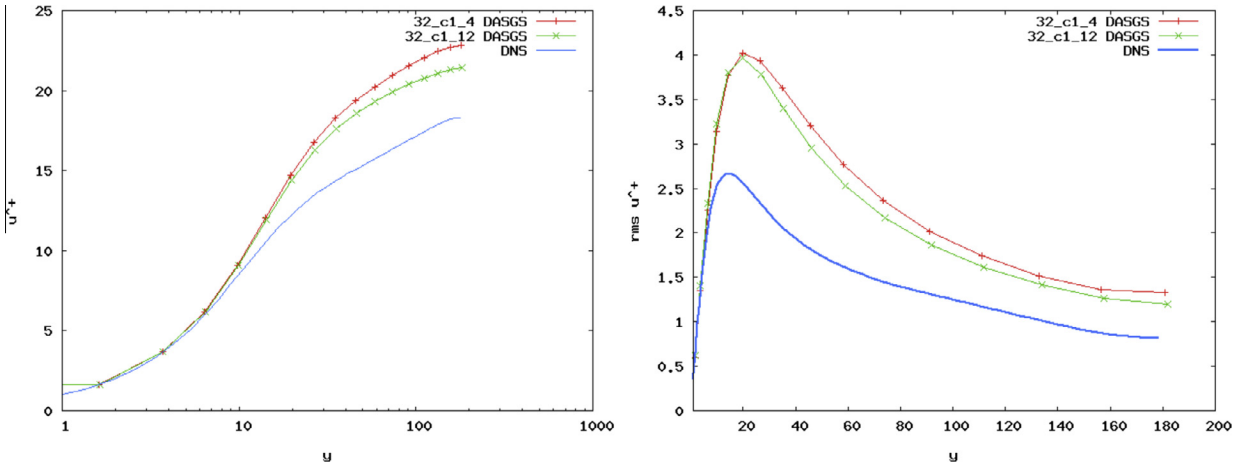

Fig. 14. Mean velocity profile (right) and its root mean square value using $c_1 = 4$ and $c_1 = 12$ for the case $T_H/T_C = 1.01$ using the DASGS method over the coarsest grid of 32^3 elements.

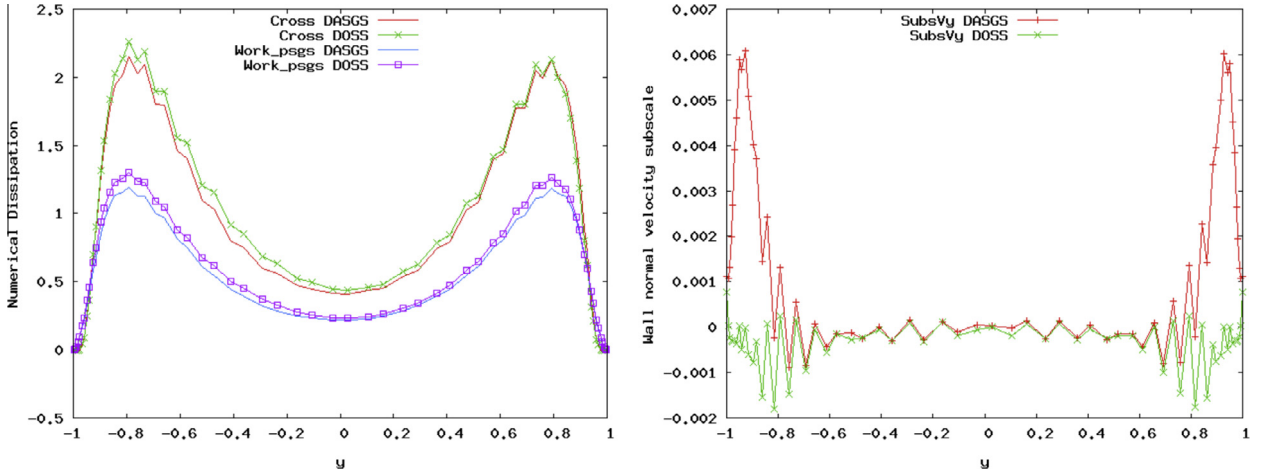

Fig. 15. Comparison of the obtained profiles of averaged numerical dissipation (left) and wall normal subgrid scale velocity (right) when using the DASGS and DOSS methods for the case $T_H/T_C = 1.01$ over the grid of 32^3 elements.

upper ($z = L_z$) and lower walls ($z = 0$), and periodic boundary conditions are imposed in x-direction. No slip velocity is imposed over all walls.

It is well known that turbulent flows driven by temperature differences are characterized by a high degree of spatial and temporal intermittency. As discussed in [29] the upstream part of the

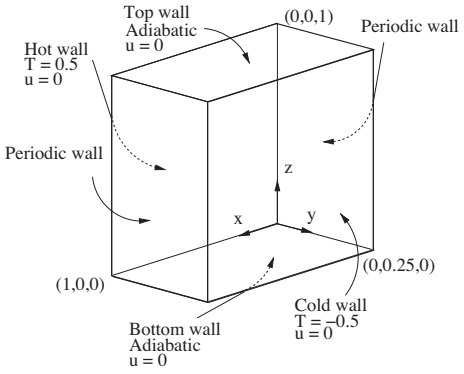

Fig. 16. Schematic of the 3D differentially heated cavity problem.

boundary layer is almost laminar and most downstream boundary layers become turbulent. Then, the small scale structures associated with turbulence are concentrated in the downstream regions of vertical boundary layers. Thus, LES of buoyant turbulent flows require accurate SGS models which are not overly dissipative and dynamically adjust in time and space to local instantaneous flow conditions. The present example is useful to test the ability of the present numerical method to adapt from laminar to transitional and turbulent flows.

The suitability of different classes of LES-SGS models has been evaluated to solve the present flow problem in [30]. In this reference LES results are compared against DNS data obtaining excellent agreement using dynamic Smagorinsky [31], the recently developed Sigma model [32] and the stretched vortex model of non eddy viscosity type [33]. The dynamic Vreman model, developed by Vreman [34], was found to be inaccurate to predict turbulent fluctuations, and not suitable to solve the present thermally coupled example. The constant coefficient Smagorinsky and constant coefficient Vreman models, which are the simplest possible versions of these respective class of models, were found to be unable to predict even the mean profiles.

The flow is governed only by two dimensionless parameters when using the Boussinesq approximation, these are the Rayleigh number (Ra) and the Prandtl number (Pr)

$$\mathrm{Ra} = \frac{|\mathbf{g}|\rho_0^2 L_z^3}{\mu^2}\varepsilon\mathrm{Pr}, \quad \mathrm{Pr} = \frac{\mu c_p}{k}$$

where μ, c_p and k denote the molecular viscosity, specific heat and heat conductivity coefficients, respectively. The dimensionless temperature ratio is $\varepsilon = \frac{T_H - T_C}{T_0}$. In the present simulation the Prandtl number is fixed to $\mathrm{Pr} = 0.71$ and two different Rayleight numbers of $\mathrm{Ra} = 6.4 \cdot 10^8$ and $\mathrm{Ra} = 2.0 \cdot 10^9$ are considered. For this configuration, the critical Ra for the transition to unsteadiness is $\mathrm{Ra} = 1.57 \cdot 10^8$. The obtained results are compared against DNS simulations carried by Trias et al. [28,29] with the Boussinesq equations.

Low Mach number flows can be approximated by the Boussinesq equations when the following two relationships are satisfied [35,36]:

$$\varepsilon \ll 1, \quad \frac{|\mathbf{g}|L_z}{c_p(T_H - T_C)} \ll 1 \tag{52}$$

The applicability of the Boussinesq-approximated and low Mach number equations on a thermal driven square cavity has been discussed in [37], where the time averaged turbulent results are compared using Boussinesq, low Mach and fully compressible simulations.

The initial conditions for thermodynamic pressure and temperature are set to $p_0^{th} = 86,100$ Pa and $T_0 = 300$ K, yielding an initial uniform density $\rho_0 = 1.0\,\mathrm{kg/m^3}$. The gas constant and specific heat capacity are respectively $R = 287.0\,\mathrm{J/(kg\,K)}$ and $c_p = 1004.5\,\mathrm{J/(kg\,K)}$. Boundary wall temperatures are $T_H = 301$ K and $T_C = 299$, with $T_0 = (T_H + T_C)/2$, giving a dimensionless temperature ratio $\varepsilon = 1/150$. The left hand side in the right condition of (52) is $\frac{|\mathbf{g}|L_z}{c_p(T_H - T_C)} = 0.053$. Therefore the low Mach flow will be appropriately approximated by the Boussinesq equation.

The reference results are presented in [27,30] in terms of the dimensionless velocity $\mathbf{u}^*$ and temperature T^*

$$\mathbf{u}^* = \frac{\mathbf{u}}{U_0}, \quad T^* = \frac{T - T_0}{T_H - T_C}$$

The properties of the problem are chosen such the reference velocity is $U_0 = \frac{\mathrm{Ra}^{1/2}k}{L_z\rho_0 c_p} = 1\,\mathrm{m/s}$ and therefore $\mathbf{u}^*$ and $\mathbf{u}$ have the same numerical value. The gravity force is $|\mathbf{g}| = 106.5\,\mathrm{m/s^2}$, the viscosity and conductivity values depend on the problem being solved as

$$\mu = \mathrm{PrRa}^{-1/2}\mu_{\mathrm{ref}}, \qquad k = \mu c_p/\mathrm{Pr}$$

where $\mu_{\mathrm{ref}} = \mathrm{Pr}^{1/2} \mid \mathbf{g}|^{-1/2}\rho_0^{-1}L_z^{-3/2}\varepsilon^{-1/2} = 1\,\mathrm{kg/(ms)}$. In this example all the results will be given in dimensionless form, but for simplicity we will omit the star over the symbols.

Two computational meshes have been used, consisting of $64 \times 64 \times 128$ and $96 \times 96 \times 192$ elements in the x, y, z directions. The coarser mesh has been used to solve the lower Rayleigh number problem $\mathrm{Ra} = 6.4 \cdot 10^8$, and the finer mesh to solve the higher Ra problem $\mathrm{Ra} = 2.0 \cdot 10^9$. Meshes with the same number of elements are used in [30] for the same two problems. They solved the higher Rayleigh number problem using also the coarser mesh of $64 \times 64 \times 128$ elements, concluding that the finer grid is required for simulating turbulent natural convection.

Grid spacing in the periodic direction is uniform and the wall-normal nodes are distributed using a hyperbolic-tangent function. The location y^j and z^j of each grid node i, j, with $i = 1,\ldots,n_y+1$ and $j = 1,\ldots,n_z+1$, where n_y and n_z are the number of elements in the y and z directions, are given by

$$y^j = \frac{L_y}{2}\left(\frac{\tanh\left(1.5\left(\frac{2(i-1)}{n_y} - 1\right)\right)}{\tanh(1.5)}\right),$$

$$z^j = \frac{L_z}{2}\left(\frac{\tanh\left(1.35\left(\frac{2(j-1)}{n_z} - 1\right)\right)}{\tanh(1.35)}\right)$$

The time step size for all simulations is $\Delta t = 0.01$ s (the dimensionless time step being $\Delta t^* = 0.01$). The simulations were carried out for 500 s for the flow to achieve a statistically stationary state, and for a further 500 s, over which time averages of velocities, temperature and other relevant quantities were collected. Statistical averaging was carried out over time, and the homogeneous x direction.

5.3.2. Mean velocity and temperature profile

The obtained mean vertical velocity and temperature profiles for DASGS and DOSS methods are compared to DNS results. Profiles near the hot wall along nine vertical locations $z = 0.1,\ 0.2,\ 0.3,\ 0.4,\ 0.5,\ 0.6,\ 0.7,\ 0.8,\ 0.9$ m are shown in Fig. 17 for the two Rayleigh numbers considered. It is observed that the obtained profiles match DNS results almost exactly. Thus, the DASGS and DOSS models are able to predict the mean profiles accurately in the near wall region. It is seen in [30] that the constant coefficient Smagorinsky and constant Vreman model are unable to predict the mean profiles accurately. It is known that Smagorinsky model introduces non-vanishing eddy-viscosity in local laminar regions, and is unable to predict the near wall behavior in both laminar and turbulent flows.

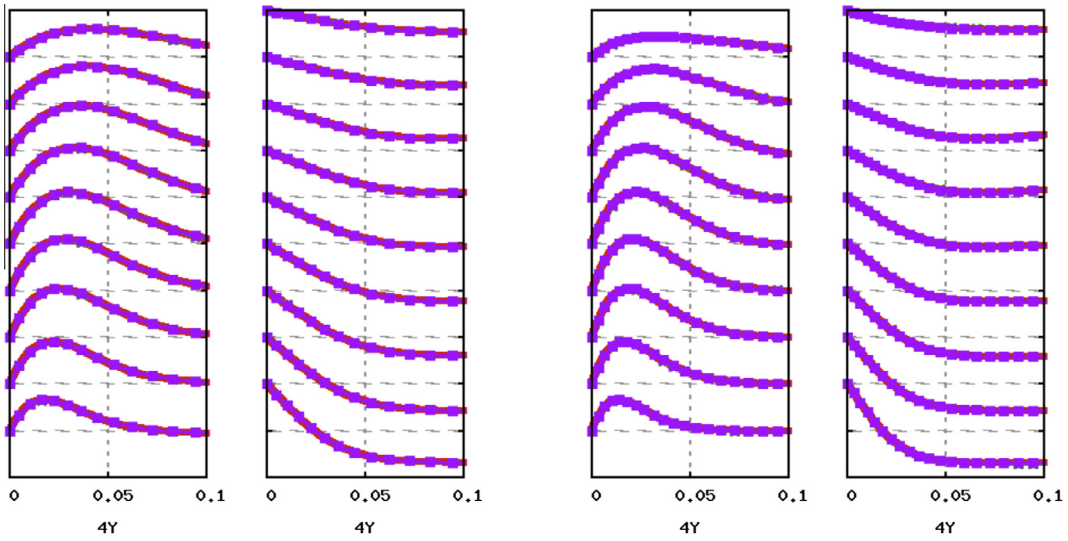

Fig. 17. Profiles of averaged vertical velocity (left hand side of each pair) and temperature (right hand side of each pair) near the wall at $z = 0.1,\ 0.2,\ 0.3,\ 0.4,\ 0.5,\ 0.6,\ 0.7,\ 0.8,\ 0.9$ m, for $\mathrm{Ra} = 6.4 \cdot 10^8$ (pair on the left) and $\mathrm{Ra} = 2.0 \cdot 10^9$ (pair on the right). Solid line: DNS, star symbols: DASGS, square symbols: DOSS. Each vertical subdivision represents 0.5 units for temperature and 0.2 units for vertical velocity. The abscissa is $4y$.

In Fig. 18 it is shown the mean vertical velocity and temperature profiles over the entire width of the cavity at location $z = 0.8$ m for both Ra numbers. It is seen that DASGS and DOSS methods are able to predict the mean profiles accurately also away from the walls. It was shown in [30] that dynamic Smagorinsky, Sigma, Dynamic Vreman and stretched vortex models are accurate at $\mathrm{Ra} = 6.4 \cdot 10^8$, but show some discrepancies with the DNS data at $\mathrm{Ra} = 2.0 \cdot 10^9$. It is seen that the numerical models developed in the present paper are able to predict better the mean values away from the wall that most LES methods.

5.3.3. Second order turbulence statistics

It is discussed in [29] that an important part of the flow remains laminar, the upstream part of the boundary layer is almost laminar and the most downstream boundary layers become turbulent. Then, turbulent fluctuations are expected to be more significant in the downstream part of the boundary layers.

The present DOSS and DASGS methods are evaluated here with regard to their ability to predict second-order turbulent statistics. The relevant turbulent statistics are velocity and temperature RMS quantities, and velocity-velocity or velocity-temperature

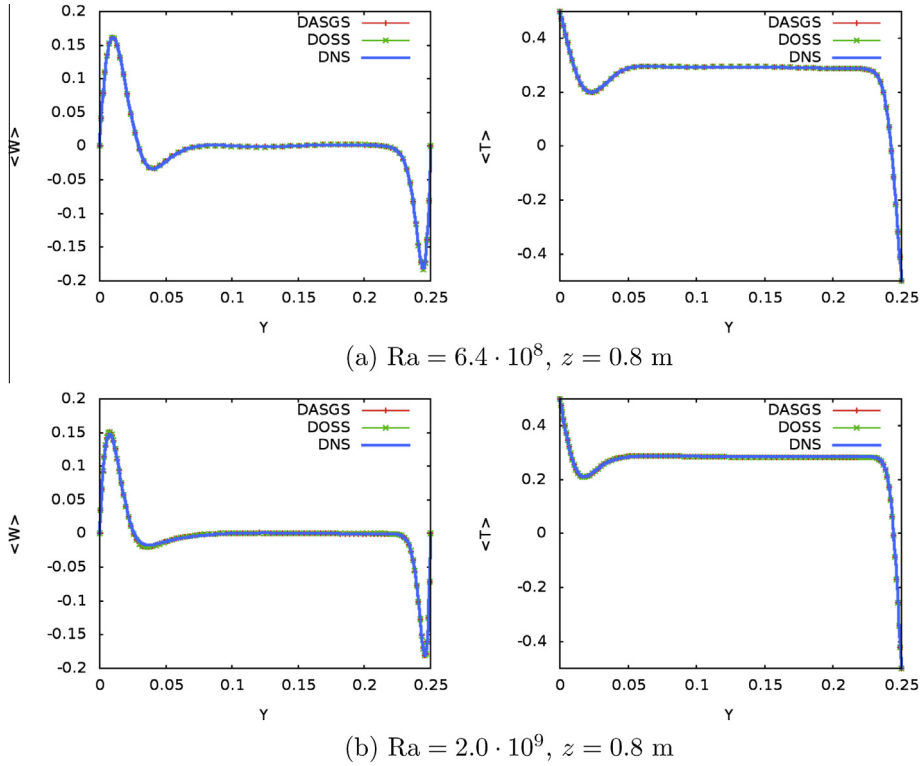

Fig. 18. Mean vertical velocity and temperature profiles for (a) $\mathrm{Ra} = 6.4 \cdot 10^8,\ z = 0.8$; (b) $\mathrm{Ra} = 2.0 \cdot 10^9,\ z = 0.8$ m.

cross correlations. Profiles of these turbulent statistics are compared to DNS results in Fig. 19 for $Ra = 6.4 \cdot 10^8$ at vertical locations $z = 0.5$ m and $z = 0.8$ m. It is observed that turbulent fluctuations are smaller at the mid vertical location ($z = 0.5$ m) than at the off-center locations ($z = 0.8$ m). It can be seen that DASGS and DOSS methods give very similar results, and both methods are excellent at predicting the turbulent statistics close to the boundaries at both vertical locations $z = 0.5$ m and $z = 0.8$ m. Due to the assumed flow symmetry about the center of the cavity, valid for Boussinesq models, the abscissa in Fig. 19 ranges until the center of the cavity ($y = 0.125$ m) when $z = 0.5$ m instead of up to the cold wall ($y = 0.25$ m) when $z = 0.8$ m. Fluctuations over the more laminar region close to the cold wall at $z = 0.8$ m are very accurately reproduced. This is not the case for the most accurate LES models analyzed in [30], which give second order statistics differing notably from DNS results close to the hot boundary at the off center location $z = 0.8$ m. Thus, close to the walls DASGS and DOSS methods predict turbulent fluctuations with much higher accuracy that all the LES models analyzed in [30]. However, away from the walls fluctuations are determined with a similar level of accuracy.

Fig. 20 shows the turbulent statistics for $Ra = 2.0 \cdot 10^9$ at vertical locations $z = 0.5$ m and $z = 0.9$ m. The behavior of our models in this case is even better than their behavior for lower Ra over

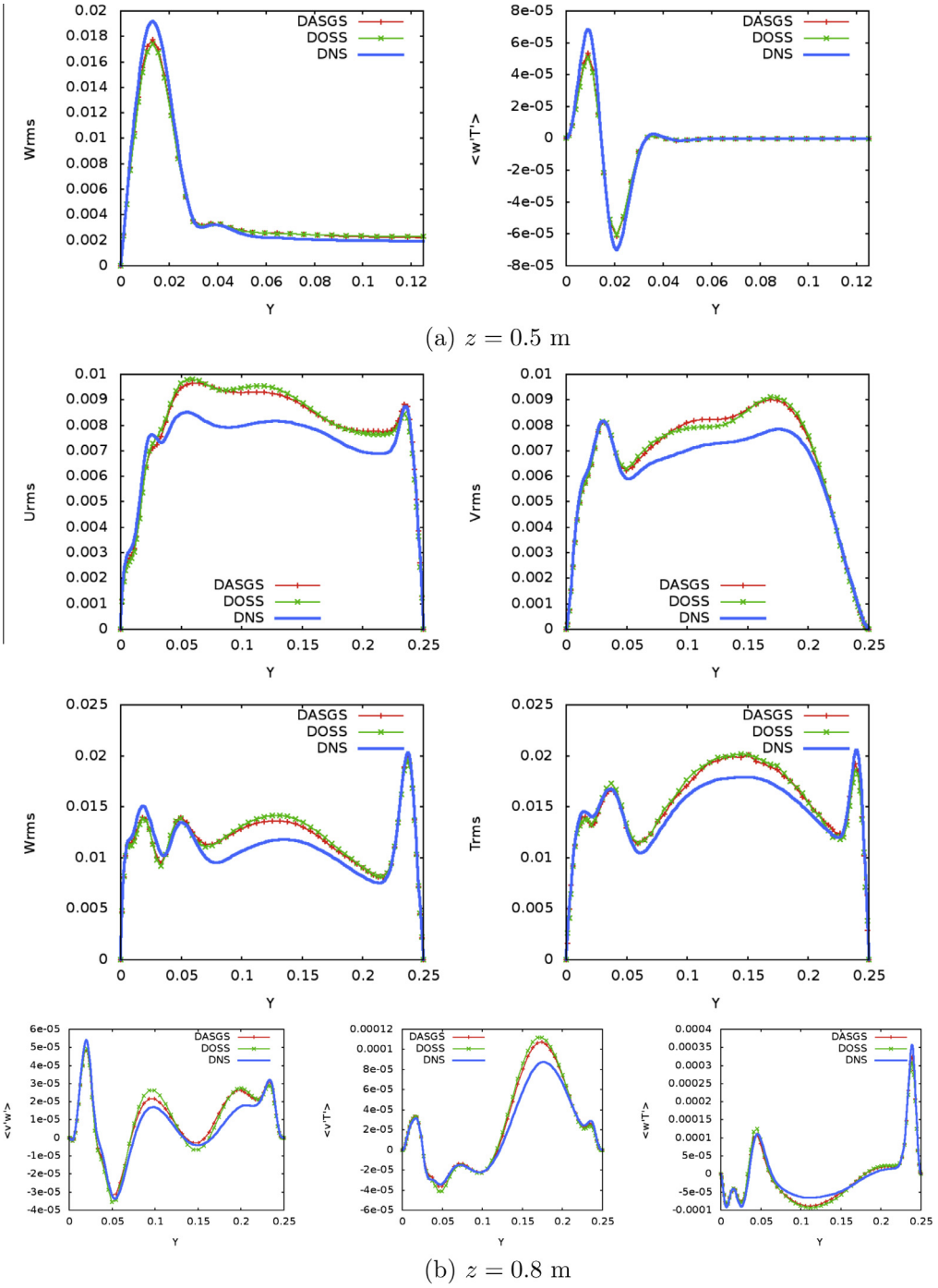

Fig. 19. Second order turbulent statistics (RMS quantities and correlations) for $Ra = 6.4 \cdot 10^8$ at (a) mid vertical location $z = 0.5$ m (b) off center location $z = 0.8$ m.

coarser mesh. The DASGS and DOSS methods give similar results, being excellent at predicting the turbulent statistics over the entire width of the cavity at both vertical locations $z = 0.5$ m and $z = 0.9$ m. All LES models analyzed by Ghaisas et al. [30] underpredict the turbulent fluctuations at the off center location $z = 0.9$ m close to the hot wall, using a mesh with the same number of degrees of freedom as the one used in the present example. For the higher Ra problem, the numerical methods DASGS and DOSS predict turbulent fluctuations with much better agreement to DNS results than all LES models analyzed in [30].

We used meshes with the same number of degrees of freedom as those used in [30], but with different near wall refinement. In order to quantify near wall resolution of the simulations, the value of the first grid point in the y-direction expressed in terms of non-dimensional wall units is plotted in Fig. 21. The viscous length scale, δ_v, used for this normalization is the same as that used in [30], given by

$$\delta_v = \left(\frac{\sqrt{\mathrm{Ra}}}{\mathrm{Pr}} \frac{\partial u_z}{\partial y}\bigg|_{y=0} \right)^{-1/2} \tag{53}$$

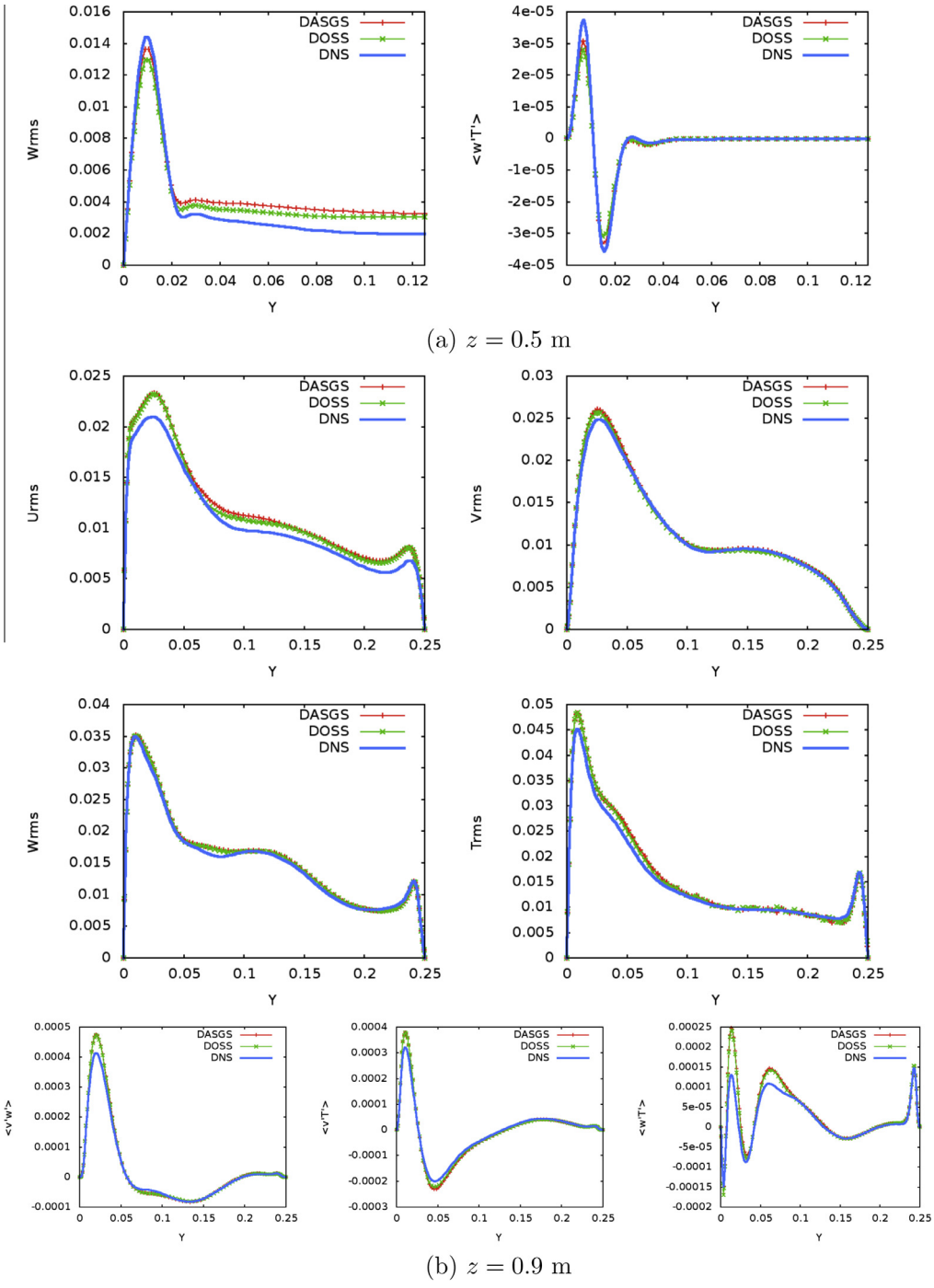

Fig. 20. Second order turbulent statistics (RMS quantities and correlations) for $\mathrm{Ra} = 2.0 \cdot 10^9$ at (a) mid vertical location $z = 0.5$ m (b) off center location $z = 0.9$ m.

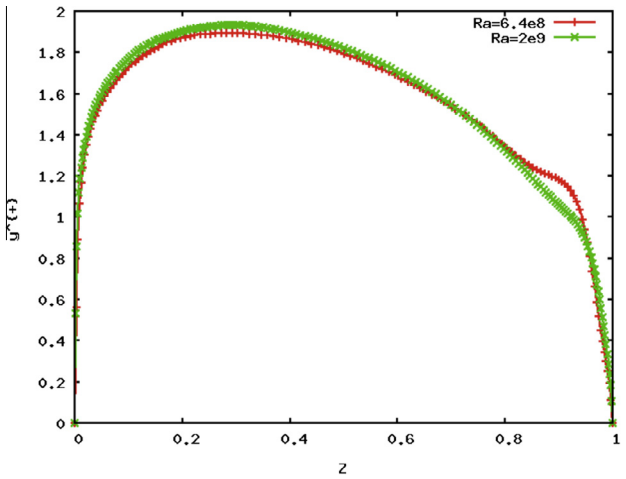

Fig. 21. Spacing of the first grid point in the y direction, expressed in terms of walls units, using the DASGS model.

Fig. 21 shows that the first grid point in y-direction is at a maximum distance of $y_1^+ \approx 1.89$ for $\mathrm{Ra} = 6.4 \cdot 10^8$ and $y_1^+ \approx 1.93$ for $\mathrm{Ra} = 2.0 \cdot 10^9$. These values are lower than those obtained by Ghaisas et al., with the first grid point in the y-direction at a maximum distance of $y_1^+ \approx 2.9$ for both Ra problems. Therefore we are using a more refined mesh close to the walls (and less refined in the center of the cavity) than the mesh used by Ghaisas. This could be a reason to obtain better results close to the walls.

5.3.4. Heat flux and stresses over the walls

The averaged local Nusselt number distribution $\left(\mathrm{Nu} = L_z \frac{\partial T^*}{\partial x}\right)$ obtained for $\mathrm{Ra} = 6.4 \cdot 10^8$ and $\mathrm{Ra} = 2.0 \cdot 10^9$ are compared to DNS results [29] in Fig. 22. It is observed in this figure that the profiles corresponding to DASGS and DOSS methods are indistinguishable from DNS results. Thus, the temperature gradients are predicted almost exactly over the wall using both DASGS and DOSS methods.

The dimensionless time-averaged vertical wall shear stress $\left(\tau = \mathrm{Ra}^{-1/4} \frac{\partial u_z}{\partial y}\right)$ obtained for $\mathrm{Ra} = 6.4 \cdot 10^8$ and $\mathrm{Ra} = 2.0 \cdot 10^9$ is compared to DNS results [28] in Fig. 23. The stress over the wall predicted by the DASGS and DOSS methods are quite close between them, and lower than DNS values. Better predictions are obtained in the downstream part of the boundary layers, and for $\mathrm{Ra} = 2.0 \cdot 10^9$.

The DASGS and DOSS models have been shown to be suitable to solve turbulent thermally driven flows. The obtained results are in very good agreement with DNS results, specially for the higher Rayleigh number case $\mathrm{Ra} = 2.0 \cdot 10^9$. For the present problem the

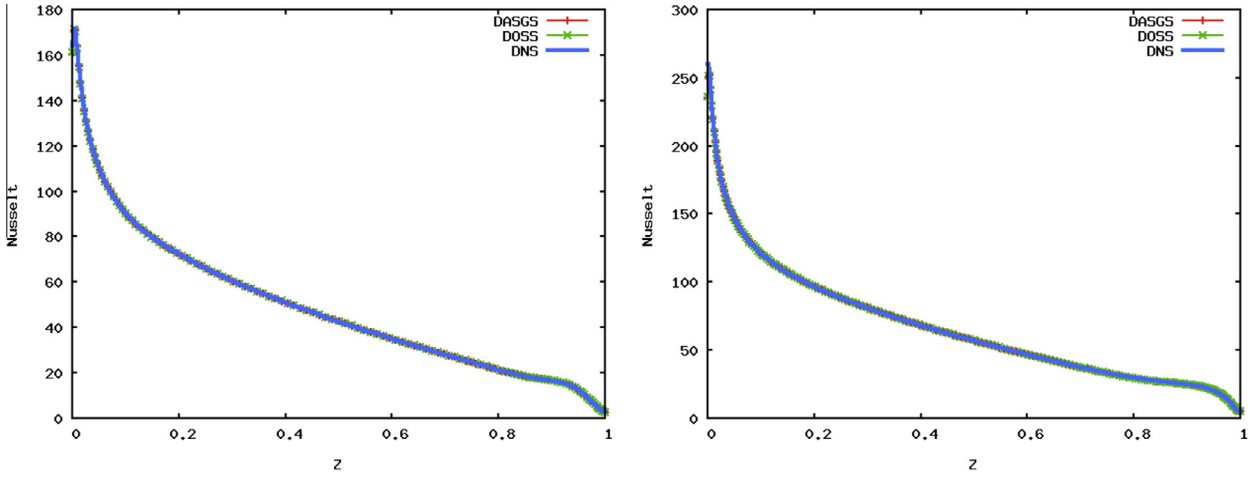

Fig. 22. Local time-averaged Nusselt number distribution for $\mathrm{Ra} = 6.4 \cdot 10^8$ (left) and $\mathrm{Ra} = 2.0 \cdot 10^9$ (right).

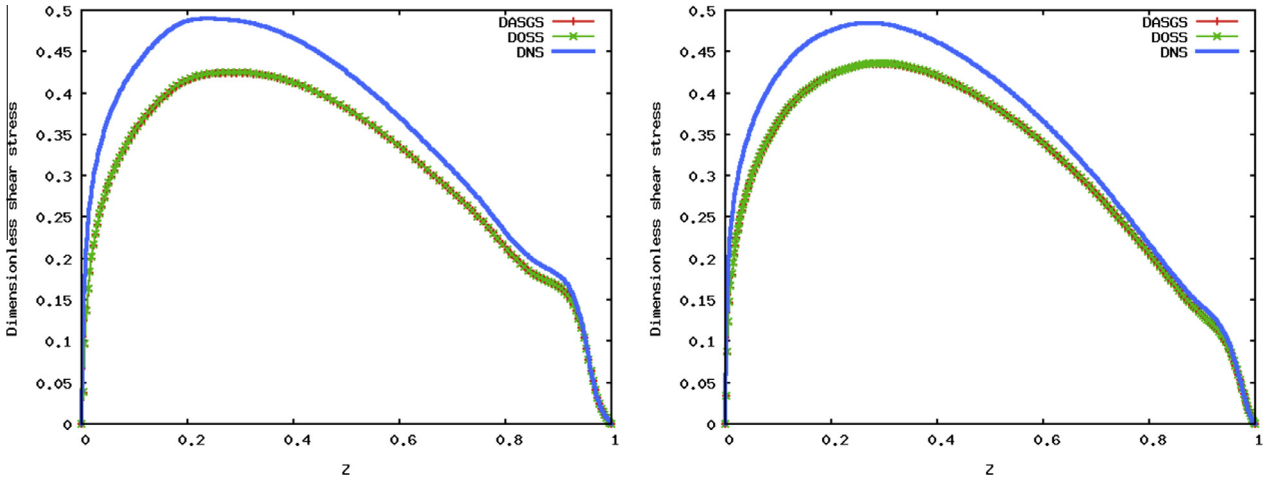

Fig. 23. Dimensionless time-averaged vertical wall shear stress scaled by $\mathrm{Ra}^{-1/4}$.

accuracy of the method has been shown to be better in some cases than that obtained using modern LES models.

6. Conclusions

In the formulation presented herein, the space of the subscales can be chosen to be orthogonal to the finite element space or to be the space of finite element residuals, leading respectively to the DOSS and the DASGS methods. In this paper we have extended the orthogonal subgrid scale method DOSS introduced in [38] and extensively applied to the incompressible Navier Stokes equations [39,3] to variable density flows. This new formulation DOSS has been shown to be more accurate and less diffusive than the DASGS formulation introduced in [2], specially in laminar problems. However, in turbulent flows the DOSS and the DASGS methods introduce similar amounts of numerical dissipation.

We have applied both the DOSS and the DASGS methods to turbulent low Mach number flow problems without introducing any additional turbulence model. In particular, the turbulent channel flow and a thermally driven cavity have been solved using *only* numerical techniques. The obtained solutions are stable and convergent to DNS values. The accuracy of the obtained results for the thermal driven cavity is even better than that obtained when using modern LES methods, as in [30]. The obtained results for the turbulent channel flow have been compared to those presented in [8], showing a similar level of accuracy. However, for the turbulent channel flow, the convergence and accuracy is not as precise as that obtained using modern LES models [20] with a proper damping close to the wall.

The dissipative structure of the formulation proposed has been analyzed, identifying its main dissipative mechanisms. A skew symmetric formulation avoiding non physical dissipation mechanisms coming from the temporal and convective terms has been proposed.

We have found for the turbulent channel flow that the numerical solutions are very sensitive to the numerical parameter c_1, which appears in the definition of the stabilization parameters τ_c, τ_m and τ_e. For linear elements (trilinear, in our examples), best results are obtained when c_1 is fixed to $c_1 = 12$, instead of $c_1 = 4$ as in [2] for laminar flows.

We believe that the material presented here is a clear indication of the potential of the method to model all kinds of turbulent thermally coupled flows. We also would like to stress that the formulation we propose is the *same* as in laminar regimes, where the improvement with respect to classical stabilized finite element methods is notorious. Having a unique formulation for all regimes is valuable *per se*.

Acknowledgements

The authors acknowledge the financial support received from the Spanish Ministry of Economics and Competitiveness, National Programme of R&D to the project PARANAT (ENE2011-28825). R. Codina also acknowledges the financial support received from the ICREA Acadèmia Program, from the Catalan Government.

References

[1] Hughes TJR, Feijóo GR, Mazzei L, Quincy J. The variational multiscale method – a paradigm for computational mechanics. Comput Methods Appl Mech Eng 1998;166:3–24.
[2] Avila M, Principe J, Codina R. A finite element dynamical nonlinear subscale approximation for the low Mach number flow equations. J Comput Phys 2011;230:7988–8009.
[3] Codina R. Stabilized finite element approximation of transient incompressible flows using orthogonal subscales. Comput Methods Appl Mech Eng 2002;191:4295–321.
[4] Codina R, Principe J, Guasch O, Badia S. Time dependent subscales in the stabilized finite element approximation of incompressible flow problems. Comput Methods Appl Mech Eng 2007;196:2413–30.
[5] Boris JP, Grinstein FF, Oran E, Kolbe RL. New insights into large eddy simulation. Fluid Dyn Res 1992;10(4–6):199.
[6] Bazilevs Y, Calo VM, Cottrell JA, Hughes TJR, Reali A, Scovazzi G. Variational multiscale residual-based turbulence modeling for large eddy simulation of incompressible flows. Comput Methods Appl Mech Eng 2007;197:173–201.
[7] Colomes O, Badia S, Codina R, Principe J. Assessment of variational multiscale models for the large eddy simulation of turbulent incompressible flows, Computer Methods in Applied Mechanics and Engineering (submitted for publication) <http://codina.rmee.upc.edu>.
[8] Gravemeier V, Wall WA. An algebraic variational multiscale-multigrid method for large-eddy simulation of turbulent variable-density flow at low Mach number. J Comput Phys 2010;229:6047–70.
[9] Guasch O, Codina R. Statistical behavior of the orthogonal subgrid scale stabilization terms in the finite element large eddy simulation of turbulent flows. Comput Methods Appl Mech Eng 2013;261–262:154–66.
[10] Principe J, Codina R, Henke F. The dissipative structure of variational multiscale methods for incompressible ows. Comput Methods Appl Mech Eng 2010;199:791–801.
[11] Codina R, Principe J, Avila M. Finite element approximation of turbulent thermally coupled incompressible flows with numerical sub-grid scale modelling. Int J Numer Methods Heat Fluid Flow 2010;20(5):492–516.
[12] Badia S, Codina R, Gutiérrez-Santacreu J. Long term stability estimates and existence of global attractors in a finite element approximation of the Navier–Stokes equations with numerical sub-grid scale modeling. SIAM J Numer Anal 2010;48:1013–37.
[13] Badia S, Codina R. On a multiscale approach to the transient Stokes problem. Transient subscales and anisotropic space–time discretization. Appl Math Comput 2009;207:415–33.
[14] Gravemeier V, Wall WA. Residual-based variational multiscale methods for laminar transitional and turbulent variable-density flow at low Mach number. Int J Numer Methods Fluids 2011;65:1260–78.
[15] Lilly D. The representation of small-scale turbulence theory in numerical simulation experiments. In: Goldstine H, editor. Proc. IBM scientific computing symp on environmental sciences; 1967.
[16] Principe J, Codina R. A stabilized finite element approximation of low speed thermally coupled flows. Int J Numer Methods Heat Fluid Flow 2007;18:835–67.
[17] Beccantini A, Studer E, Gounand S, Magnaud JP, Kloczko T. Numerical simulations of a transient injection flow at low Mach number regime. Int J Numer Methods Eng 2008;76:662–96.
[18] Nicoud F. Conservative high-order finite-difference schemes for low-Mach number flows. J Comput Phys 2000;158:71–97.
[19] Nicoud F. Numerical study of a channel flow with variable properties. In: Annual research briefs. Center for Turbulence Research; 1998.
[20] Lessani B, Papalexandris MV. Time-accurate calculation of variable density flows with strong temperature gradients and combustion. J Comput Phys 2006;212(1):218–46.
[21] Wang W, Pletcher RH. On the large eddy simulation of a turbulent channel flow with significant heat transfer. Phys Fluids 1996;8(12):3354–66.
[22] Moser RD, Kim J, Mansour NN. Direct numerical simulation of turbulent channel flow up to $Re_\tau = 590$. Phys Fluids 1999;11(4):943–5.
[23] Speziale CG. Analytical methods for the development of Reynolds-stress closures in turbulence. Ann Rev Fluid Mech 1991;23(1):107–57.
[24] Trofimova AV, Tejada-Martínez AE, Jansen KE, Lahey Jr RT. Direct numerical simulation of turbulent channel flows using a stabilized finite element method. Comput Fluids 2009;38(4):924–38.
[25] Nicoud F, Poinsot T. DNS of a channel flow with variable properties. In: Int symp on turbulence and shear flow phenomena; 1999. p. 12–15.
[26] Codina R. A stabilized finite element method for generalized stationary incompressible flows. Comput Methods Appl Mech Eng 2001;190(20–21):2681–706.
[27] Trias F, Soria M, Oliva A, Pérez-Segarra C. Direct numerical simulations of two- and three-dimensional turbulent natural convection flows in a differentially heated cavity of aspect ratio 4. J Fluid Mech 2007;586:259–93.
[28] Trias F, Gorobets A, Soria M, Oliva A. Direct numerical simulation of a differentially heated cavity of aspect ratio 4 with Rayleigh numbers up to 1011. Part 1: Numerical methods and time-averaged flow. Int J Heat Mass Transfer 2010;53(4):665–73.
[29] Trias F, Gorobets A, Soria M, Oliva A. Direct numerical simulation of a differentially heated cavity of aspect ratio 4 with Rayleigh numbers up to 1011. Part 2: Heat transfer and flow dynamics. Int J Heat Mass Transfer 2010;53(4):674–83.
[30] Ghaisas NS, Shetty DA, Frankel SH. Large eddy simulation of thermal driven cavity: evaluation of sub-grid scale models and flow physics. Int J Heat Mass Transfer 2013;56(12):606–24.
[31] Lilly D. A proposed modification of the Germano sub-grid scale closure method. Phys Fluids 1992;3. 663-635.
[32] Nicoud F, Toda HB, Cabrit O, Bose S, Lee J. Using singular values to build a subgrid-scale model for large eddy simulations. Phys Fluids 2011;23(8):085–106.
[33] Misra A, Pullin DI. A vortex-based subgrid stress model for large-eddy simulation. Phys Fluids 1997;9(8):2443–54.

[34] Vreman AW. An eddy-viscosity subgrid-scale model for turbulent shear flow: algebraic theory and applications. Phys Fluids 2004;16(10):3670–81.
[35] Principe J, Codina R. Mathematical models for thermally coupled low speed flows. Adv Theor Appl Mech 2009;2:93–112.
[36] Tritton DJ. Physical fluid dynamics. Oxford University Press; 1999.
[37] Mlaouah H, Tsuji T, Nagano Y. A study of non-Boussinesq effect on transition of thermally induced flow in a square cavity. Int J Heat Fluid Flow 1997;18(1):100–6.
[38] Codina R. Stabilization of incompressibility and convection through orthogonal sub-scales in finite element methods. Comput Methods Appl Mech Eng 2000;190(13–14):1579–99.
[39] Codina R. Analysis of a stabilized finite element approximation of the Oseen equations using orthogonal subscales. Appl Numer Math 2008;58:264–83.